ANALYSIS AND CONTROL OF A RUNNING SPRING-MASS MODEL WITH AN UPRIGHT TRUNK BASED ON VIRTUAL PENDULUM CONCEPT

A THESIS SUBMITTED TO
THE GRADUATE SCHOOL OF NATURAL AND APPLIED SCIENCES
OF
MIDDLE EAST TECHNICAL UNIVERSITY

BY

OSMAN KAAN KARAGÖZ

IN PARTIAL FULFILLMENT OF THE REQUIREMENTS
FOR
THE DEGREE OF MASTER OF SCIENCE
IN
ELECTRICAL AND ELECTRONICS ENGINEERING

SEPTEMBER 2020

Approval of the thesis:

ANALYSIS AND CONTROL OF A RUNNING SPRING-MASS MODEL WITH AN UPRIGHT TRUNK BASED ON VIRTUAL PENDULUM CONCEPT

submitted by **OSMAN KAAN KARAGÖZ** in partial fulfillment of the requirements for the degree of **Master of Science in Electrical and Electronics Engineering Department, Middle East Technical University** by,

Prof. Dr. Halil Kalıpçılar
Dean, Graduate School of **Natural and Applied Sciences** ______________

Prof. Dr. İlkay Ulusoy
Head of Department, **Electrical and Electronics Engineering** ______________

Assist. Prof. Dr. Mustafa Mert Ankaralı
Supervisor, **Electrical and Electronics Engineering, METU** ______________

Prof. Dr. Uluç Saranlı
Co-supervisor, **Computer Engineering, METU** ______________

Examining Committee Members:

Prof. Dr. Klaus Werner Schmidt
Electrical and Electronics Engineering, METU ______________

Assist. Prof. Dr. Mustafa Mert Ankaralı
Electrical and Electronics Engineering, METU ______________

Prof. Dr. Uluç Saranlı
Computer Engineering, METU ______________

Assoc. Prof. Dr. Yiğit Yazıcıoğlu
Mechanical Engineering, METU ______________

Assist. Prof. Dr. İsmail Uyanık
Electrical and Electronics Engineering, Hacettepe University ______________

Date:07.09.2020

I hereby declare that all information in this document has been obtained and presented in accordance with academic rules and ethical conduct. I also declare that, as required by these rules and conduct, I have fully cited and referenced all material and results that are not original to this work.

Name, Surname: Osman Kaan Karagöz

Signature :

ABSTRACT

ANALYSIS AND CONTROL OF A RUNNING SPRING-MASS MODEL WITH AN UPRIGHT TRUNK BASED ON VIRTUAL PENDULUM CONCEPT

Karagöz, Osman Kaan
M.S., Department of Electrical and Electronics Engineering
Supervisor: Assist. Prof. Dr. Mustafa Mert Ankaralı
Co-Supervisor: Prof. Dr. Uluç Saranlı

September 2020, 58 pages

Spring-Loaded Inverted Pendulum (SLIP) is widely used in locomotion community to analyze the running behavior of legged animals and design controllers by embedding its dynamics as a template model. It is a conceptual model composed of a mass-less ideal compliant leg attached to a point mass. Although the SLIP model can adequately explain the center of mass trajectories of legged animals, there have been some cases where this model remains insufficient while embedding into real platforms because of its over-simplified structure. Over the years, researchers have proposed various extensions to the SLIP model, such as torque actuation and damping, to adopt SLIP for physical platforms. In addition to these, another critical extension to the SLIP model is a rigid trunk that stands for upper body dynamics, which are unavoidable in systems that have body mass far from the hip joint like humanoid robots. In this context, researchers have developed several methods and algorithms to stabilize and regulate the trunk extended SLIP like systems. One of these control schemes is called the Virtual Pivot Point (VPP) concept, and it will be one of the focal points of this thesis.

In this thesis, we present a comprehensive analysis of the VPP concept. We systematically analyze the periodic solutions of this concept for running behavior. We extract periodic solutions for different states and parameters of the system using numeric analysis tools. And then, we compare the characteristic of periodic solutions among themselves based on metrics such as energy efficiency and stability. Finally, we develop a new controller to stabilize the system dynamics. We compare this new control policy with an extended version of a controller introduced by Sharbafi et al. (2013) for the VPP framework. We demonstrate the effectiveness of both controllers and find that the proposed controller can create a larger basin of attractions for different periodic solutions without compromising from the convergence speed performance. After all, this thesis shows that the VPP concept, in conjunction with the proposed controller, could be beneficial in the design and control of legged robots targeting running behavior with non-trivial upper body dynamics.

Keywords: legged locomotion, spring loaded inverted pendulum model, poincaré map method, periodic solution analysis, linear quadratic regulator, humanoid robots

ÖZ

SANAL SARKAÇ KAVRAMINA DAYALI DİK GÖVDE İLE KOŞAN YAY-KÜTLE MODELİNİN ANALİZİ VE KONTROLÜ

Karagöz, Osman Kaan
Yüksek Lisans, Elektrik ve Elektronik Mühendisliği Bölümü
Tez Yöneticisi: Dr. Öğr. Üyesi. Mustafa Mert Ankaralı
Ortak Tez Yöneticisi: Prof. Dr. Uluç Saranlı

Eylül 2020 , 58 sayfa

Yaylı Ters Sarkaç (SLIP), dinamiklerini bir şablon modeli olarak gömerek bacaklı hayvanların koşma davranışını analiz etmek için ve denetleyicilerin tasarımında yaygın olarak kullanılır. Bir nokta kütleye tutturulmuş kütlesiz ideal esnek bir bacaktan oluşan kavramsal bir modeldir. SLIP modeli, bacaklı hayvanların kütle merkezinin yörüngelerini yeterince açıklayabilse de, bu modelin fazla basitleştirilmiş yapısı nedeniyle gerçek platformlara gömülürken yetersiz kaldığı bazı durumlar olmuştur. Yıllar boyunca araştırmacılar, SLIP modelini fiziksel platformlara daha uygun hale getirmek için SLIP modeline eyleyici ve sönümleme gibi çeşitli uzantılar önerdiler. Bunlara ek olarak, SLIP modelinin bir diğer kritik uzantısı, insansı robotlar gibi kalça ekleminden uzak vücut kütlesine sahip sistem1lerde kaçınılmaz olan, üst vücut dinamiklerini temsil eden bir gövdedir. Bu bağlamda, araştırmacılar gövde eklenerek genişletilmiş SLIP benzeri sistemleri stabilize etmek ve düzenlemek için çeşitli yöntemler ve algoritmalar geliştirmişlerdir. Bu kontrol şemalarından biri Sanal Pivot Noktası (VPP) kavramı olarak adlandırılır ve bu tezin odak noktalarından biridir.

Bu tezde, VPP konseptinin kapsamlı bir analizini sunuyoruz. Koşu davranışı için

bu konseptin periyodik çözümlerini sistematik olarak analiz ediyoruz. Sayısal analiz araçlarını kullanarak sistemin farklı durumları ve parametreleri için periyodik çözümler çıkarıyoruz. Ardından, enerji verimliliği ve kararlılık gibi metriklere göre periyodik çözümlerin özelliklerini kendi aralarında karşılaştırıyoruz. Son olarak, sistem dinamiklerini kararlı hale getirmek için yeni bir denetleyici geliştiriyoruz. Bu yeni denetleyiciyi, Sharbafi ve diğerleri (2013) tarafından sunulan bir denetleyicinin genişletilmiş bir versiyonu ile karşılaştırıyoruz. Her iki denetleyicinin etkinliğini gösteriyoruz ve önerilen denetleyicinin yakınsama hızı performansından ödün vermeden farklı periyodik çözümler için daha büyük bir çekim havuzu oluşturabileceğini gösteriyoruz. Sonuçta, bu tez, önerilen denetleyici ile birlikte VPP konseptinin, kayda değer üst vücut dinamikleri ile koşma davranışını hedefleyen bacaklı robotların tasarımında ve kontrolünde faydalı olabileceğini göstermektedir.

Anahtar Kelimeler: bacaklı hareket, yay yüklü ters sarkaç modeli, poincar é harita yöntemi, periyodik çözüm analizi, doğrusal kuadratik düzenleyici, insansı robotlar

To my family

ACKNOWLEDGMENTS

First and foremost, I would like to express my sincere appreciation and gratitude to my supervisors, Assist. Prof. Dr. Mustafa Mert Ankaralı and Prof. Dr. Uluç Saranlı, for their support, encouragement, and invaluable guidance throughout this work. It was a great opportunity for me to be guided by their knowledge and wisdom in my academic life.

I have been fortunate to work with an amazing group of people in Autonomous Technologies for Robotic Locomotion and Sensing (ATLAS) Laboratory. First of all, I am grateful to Görkem Seçer for his help and guidance in this work. Also, I am very thankful to Abdullah Cem Önem, Başer Kandehir, Ferhat Gölbol, Halil İbrahim Uğurlu, İzel Sever, JeanPiere Demir, Simay Atasoy, and Sinan Şahin Candan. They made the last three years easier not only with their intellectual knowledge but also with their great personalities.

I am thankful for the financial support from the National Scientific and Technological Research Council of Turkey (TÜBİTAK) through 2210 M.S. scholarship program and project 117E106.

Last but not the least, I want to express the deepest gratitude to my parents, Ayşe Karagöz and İrfan Karagöz, and my brothers, Ahmet E. Karagöz and Ömer E. Karagöz, for their unconditional support, encouragement, and understanding. This thesis would not have been possible without them.

TABLE OF CONTENTS

LIST OF TABLES

TABLES

LIST OF FIGURES

FIGURES

LIST OF ABBREVIATIONS

ABBREVIATIONS	
VPP	Virtual Pivot Point
SLIP	Spring Loaded Inverted Pendulum
T-SLIP	Trunk-SLIP
LQR	Linear Quadratic Regulator
PD	Proportional-Derivative
CoM	Center of Mass
CoT	Cost of Transport
GRF	Ground reaction force
TD	Touch-down
LO	Lift off
1D	1 Dimensional
3D	3 Dimensional
4D	4 Dimensional

LIST OF VARIABLES

VARIABLES

m	Mass of body
I	Inertia of body
r	Leg length
α	Leg angle
d_{vpp}	Virtual Pivot Point distance parameter
θ_{vpp}	Virtual Pivot Point angle parameter
d_{hip}	distance between hip and CoM
g	Gravitational acceleration
z	Position of body in z-direction
x	Positon of body in x-direction
θ	Body angle
ψ	Angle between body and leg
k	Spring coefficient of leg
d	Damping coefficient of leg
τ	Torque applied by hip actuation
$\mathbf{X}$	Apex state
$\mathbf{u}$	Input
F_r	Leg force
$\mathbf{q}$	Generalized coordiantes of T-SLIP Model
$\mathcal{H}$	The cost of optimization function to find fixed-points
ϕ	Phase of the T-SLIP Model

CHAPTER 1

INTRODUCTION

1.1 Motivation and Background

Although one of the key defining features that separate hominids from other primates is bipedalism, the reason behind the shifting to bipedalism is still a mystery. While some researchers argue that human bipedalism is due to an adaptation for locomotion in trees [2, 3], Some researches showed that human walking consumes less energy than chimpanzee quadrupedal or bipedal walking [4, 5]. On the other hand, there is an approach saying that bipedalism helps to stay cool by reducing the surface area exposed to direct sunlight in the hot climate of Africa [6]. Although the reason for the evolutionary transition to bipedalism is not entirely clear, bipedal humanoid robots with human-like morphology and movement abilities will naturally adapt better to complex environments, vehicles, and equipment adapted for human use [7].

Honda introduced the first autonomous walking bipedal humanoid robot in 1996 after ten years of development [8] and paved the way for a new era of humanoid robots. Honda continued to develop, and in 2000 this autonomous bipedal was named ASIMO, becoming one of the most famous humanoid robots in the world. ASIMO uses the Zero Moment Point (ZMP) method to generate a stable walking trajectory [9], and this method has been the main driving force for generating walking patterns for many different robots since then [10, 11, 12]. Even though ZMP can generate stable walking behavior, the robots that use this method are slow, and their energy efficiency is remarkably low. For example, ASIMO uses 10 times energy as human do [13].

On the other hand, Raibert, who designed a robot that looks like a pogo-stick, has shown that agile and designing robots with passive elastic materials and some intuitive controllers can lead efficient dynamic legged locomotion behaviors. [14]. The robot designed by Raibert was structurally similar to the Spring Inverted Pendulum (SLIP) model, which effectively explains the running behavior of legged animals [15]. The success of Raibert led to studies on the theoretical background for the SLIP model [16] and similar robot platforms [17, 18] with intuitive controllers.

Although these platforms have superior dynamic mobility and efficiency compared to other terrestrial platforms, they have dynamics that include non-linear, complex, and hybrid elements [19, 20, 21]. To overcome these difficulties while designing a legged robot, Full & Koditschek [22], proposed a hierarchical control structure. In this framework, while simple yet effective models called "templates" explain targeted behavior such as running and walking, complex models called "anchors" account for real or complex systems. Creating or finding policies on anchor so that anchor behaves like a template establishes the connection between a template and an anchor. This structure enables to use of simpler models like SLIP to control legged robots [23, 24, 25, 26, 27]. Within this framework, the SLIP model has become one of the most well-known, successful templates adopted as a control target for running behavior [28, 29, 30].

Although the SLIP model can adequately define the evolution of COM trajectories, it does not provide a framework for stabilizing the upper body's angular dynamics, which cannot be neglected in the systems such as bipedal humanoid robots. Moreover, significant inertial dynamics of the upper body can create even bigger problems since most of these platforms are underactuated. Indeed, the first examples of this framework in which the SLIP model is used as the control target are far from bipedal humanoid robots. Either they do not have a trunk or their CoM coincident with the hip joint. So, the embedding controllers do not have to deal with upper body dynamics in these platforms. Using simple methods such as PD (Proportional, Derivative) controller [14, 26, 31, 32], passive stability [17], gyro-stabilizer [33] could yield sufficient results for these systems. However, when such methods are used in real systems with non-trivial upper body dynamics, it becomes difficult to track the center of mass trajectories defined by the SLIP model [34]. Moreover, instead of SLIP, more inclusive templates that include body dynamics may be viable alternatives in terms of robustness, energetic efficiency, or computational load. In the next section, we mention the methods and models that account for upper body dynamics.

1.2 Existing Works

Poulakakis & Grizzle introduced the first template model, Asymmetric-SLIP[1](A-SLIP), that integrates the upper body dynamics into a SLIP-like model [35]. Fig. 2.1(a) illustrates this template model. Poulakakis & Grizzle [35] also proposed a hierarchical control structure that can potentially both stabilize the body dynamics as well as the locomotion in the same study. At the first level, they apply a high gain continuous control policy at the stance phase to maintain the body around the desired posture and create an invariant manifold on which SLIP like dynamics can be applied. At the second level, they used a gait level SLIP based controller to regulate the locomotion.

Bayir proposed PD controller to stabilize upper body dynamics [37]. They used a similar model to the T-SLIP called Body-Attached SLIP (BA-SLIP). They showed that the periodic solutions corresponding to upward body orientation are unstable with the PD controller scheme. They proposed time-varying control strategies to stabilize these periodic solutions.

In our recent work, on the T-SLIP model, we proposed a hip torque that directs all ground reaction forces to the CoM to develop different controllers for the rotational and euclidean dynamics [38]. A PD controller acts at a low-level to stabilize pitch dynamics. A high-level LQR controller stabilizes other degrees of freedom. We showed that the purposed control policy could be beneficial in designing and controlling humanoid robotic systems.

Until now, we summarized the methods that are in the literature. The approach that we focus on this thesis is called Virtual Pivot Point. We will first investigate and analyze this concept in detail and then introduce some control policy schemes for the T-SLIP model and VPP approach. Maus et al. first introduced this method on a similar model to T-SLIP in [39], and later discovered a biological basis for this concept [1]. They

[1] While Poulakakis and Grizzle refer to this template as A-SLIP [35], Sharbafi et al. use Trunk-SLIP (T-SLIP) [36]. We also prefer to use T-SLIP throughout this thesis.

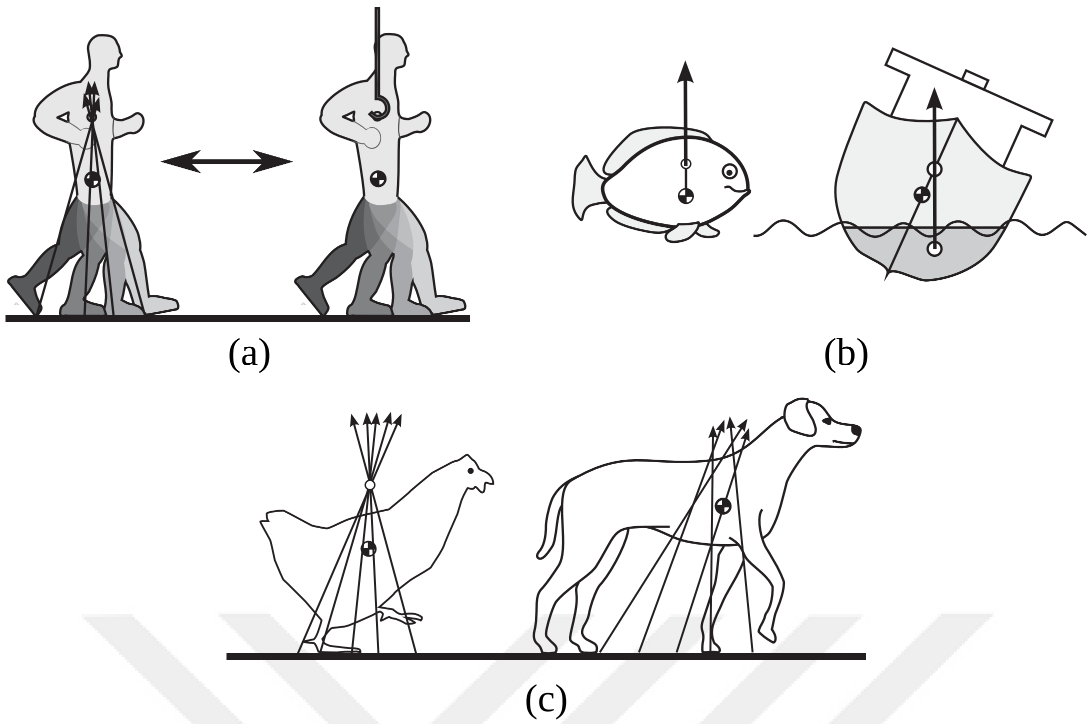

Figure 1.1: The Trunk-SLIP model. a) Virtual Pivot Point in human walking, b)Virtual Pivot Point in different platforms, c) Virtual Pivot Point in chicken running and dog walking. Retrieved from [1]

show that this concept could arise from morphologically different legged animals and different behaviors such as human walking, chicken running, and dog walking (see Fig. 1.1a and Fig. 1.1c).

The main idea behind this concept is to create a point above the COM location where all the ground reaction forces pass through so that the CoM hangs like a pendulum below this point, which could result in an inherently stable upright posture (see Fig. 1.1a). They also reported that this is not a particular case for animals, as it is possible to observe on different platforms (see Fig. 1.1b). Independent from these studies, Gurben [40] showed a similar ground reaction pattern in human walking to the VPP concept. Later on, Sharbafi et al. proposed a control approach to stabilize the hopping behavior using this concept [36]. In addition to the T-SLIP model, they also tested the algorithms in a more parsimonious template model called XT-SLIP (eXtended-TSLIP, T-SLIP with leg damping and mass).

1.3 Contributions

Analysis of the existence and characteristics of periodic solutions for systems like the T-SLIP model is vital as it guides engineers and researchers to develop energy-efficient and robust platforms and controllers without opposing the conditions dictated by the natural dynamics of the system. Simultaneously, such an analysis allows us to design control policies around these trajectories since the presence of a periodic solution brings a mathematical explanation to the system's behavior. Therefore, we systematically investigated the existence and characteristics of the periodic solutions of the VPP concept for running behavior. To the best of our knowledge, this work is the first systematic study on the VPP concept focused on periodic solutions and their characteristics. For example, Maus et al. [39] show only one regular solution for running, and Sharbafi et al. [36] present only one periodic solution for hopping behaviors.

In this thesis, we also compare the extracted periodic solutions based on the cost of transport and stability metrics. We investigate the stability of periodic solutions by using the commonly used Poincaré Map-based methods [41, 42, 43].

Lastly, we purpose a new controller called Parameterized Torque Control. We compare this new control policy with a modified version of a controller introduced by Sharbafi et al. for the VPP framework [36]. We demonstrate both controllers' effectiveness and find that the proposed controller can create a larger basin of attractions for different periodic solutions without compromising convergence speed performance.

1.4 Organization of Thesis

In Chapter 2, we cover the mathematical details of the T-SLIP model and VPP concept and briefly explain the Poincare Map Method.

In Chapter 3, we analyze the periodic solution. We show the periodic solutions' characteristics and examine the dependence of the periodic solutions on the parameters of the VPP concept.

In Chapter 4, we first give mathematical background for the controllers. Then, we introduce our controller as well as VPPC.

In Chapter 5, we show the effectiveness of both controllers and compare them with respect to the basin of attraction and the settling time.

In Chapter 6, we summarize key results and mention possible future work.

CHAPTER 2

GENERAL FRAMEWORK FOR RUNNING WITH UPRIGHT TRUNK

In this chapter, we introduce Trunk-SLIP Model and then explain the VPP concept in detail. We finalize the section with a brief explanation of the Poincaré Return Map Method, one of the most common tools adopted for the analysis and control of rhythmic dynamical systems.

2.1 Trunk-SLIP Model

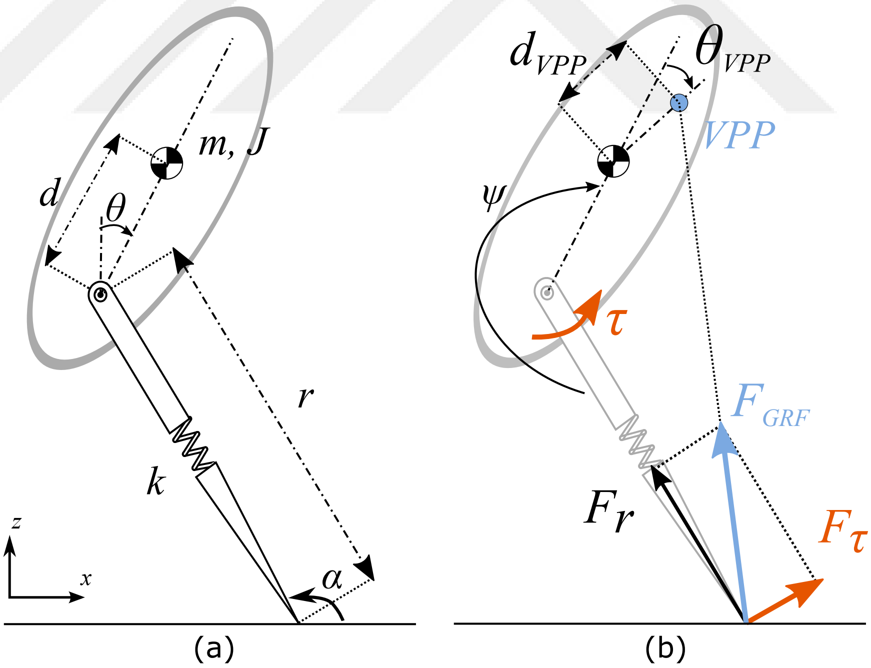

Figure 2.1: The Trunk-SLIP model. a) Physical parameters, b) Virtual Pivot Point concept, the forces and the torque acting on the model

Trunk-SLIP (T-SLIP) model is a more comprehensive & parsimonious model compared to the SLIP model for physical systems with non-trivial upper body dynamics. T-SLIP has a hip joint that does not coincide with the center of mass (CoM) of the body with mass m and inertia J, see Fig. 2.1(a). The model has a mass-less leg that acts like a radial spring, k. The only controllable actuation in the model is the torque at the hip joint. Table 2.1 presents the definitions of the variables and parameters for the model given in Fig. 2.1a. We adopted the physical parameters' values from [39], and throughout this dissertation, all the physical parameters are kept constant.

T-SLIP model has two phases, flight, and stance (see Fig. 2.2). In both phases, the model has 3 degrees of freedom. $\mathbf{q} = [x,\ z,\ \theta]^T \subseteq \mathbb{R}^2 \times S$ defines the generalized coordinates of the model. In the flight phase, the center of mass follows a ballistic trajectory which is defined by

$$\ddot{\mathbf{q}} = \mathbf{f}_f(\mathbf{q}) = \begin{bmatrix} 0 \\ -g \\ 0 \end{bmatrix}. \tag{2.1}$$

When the leg contacts the ground, the touchdown event triggers the transition to the stance phase. During this phase, we assume that the contact position does not slip. Hence the touchdown point acts like a revolute joint. The equations of motion for the stance phase take the form of

$$\ddot{\mathbf{q}} = \mathbf{f}_s(\mathbf{q}) = \begin{bmatrix} 1/m & 0 & 0 \\ 0 & 1/m & 0 \\ 0 & 0 & 1/J \end{bmatrix} \left(D_q\psi\ \tau + D_q r\ F_r - \begin{bmatrix} 0 \\ mg \\ 0 \end{bmatrix} \right), \tag{2.2}$$

where F_r, τ, ψ are leg force, hip torque and body-leg angle, respectively (see Fig. 2.1(b) and Table 2.1). $D_q\psi$ and $D_q r$ stand for Jacobian (column) matrices whose elements are the derivatives of ψ and r with respect to state variables, q, respectively (details in Appendix A). Since the leg consists of a mass-less linear spring, $F_r = -k(r - r_0)$ defines the leg force. Also, Eq. (2.2) results in non-integrable stance dynamics [44].

Fig. 2.2 illustrates the single-step evolution of T-SLIP model. In Fig. 2.2, the system/-model starts at flight phase. In this phase, we assume that we can select the touchdown angle arbitrarily in line with similar modeling frameworks in the literature [45, 46]. In this phase, hip torque activation is deactivated in the model. However, one should note that in physical systems, the leg will not be massless, and a feedback controller would need to regulate the touchdown angle via the hip torque actuation. The transition from flight to stance happens when the system trajectories cross the manifold which is defined by

$$S_{f\to s} \;\; = \;\; \{(\mathbf{q},\dot{\mathbf{q}}) \mid z - d_{hip}\, cos(\theta) - r\, cos(\alpha) = 0\} \; . \tag{2.3}$$

After the touchdown event, the system switches to the stance phase. In the stance phase, the hip torque is activated. We will use the torque actuation to realize the VPP control concept. The stance phase ends when the system crosses a manifold which is defined by

$$S_{f\to s} \;\; = \;\; \{(\mathbf{q},\dot{\mathbf{q}}) \mid F^{z}_{GRF} = 0 \; \} \; . \tag{2.4}$$

where F^{z}_{GRF} stands for the vertical component of the GRF and we evaluate as $F^{z}_{GRF} = [0,\ 1,\ 0] \cdot \mathbf{f}_s + mg$.

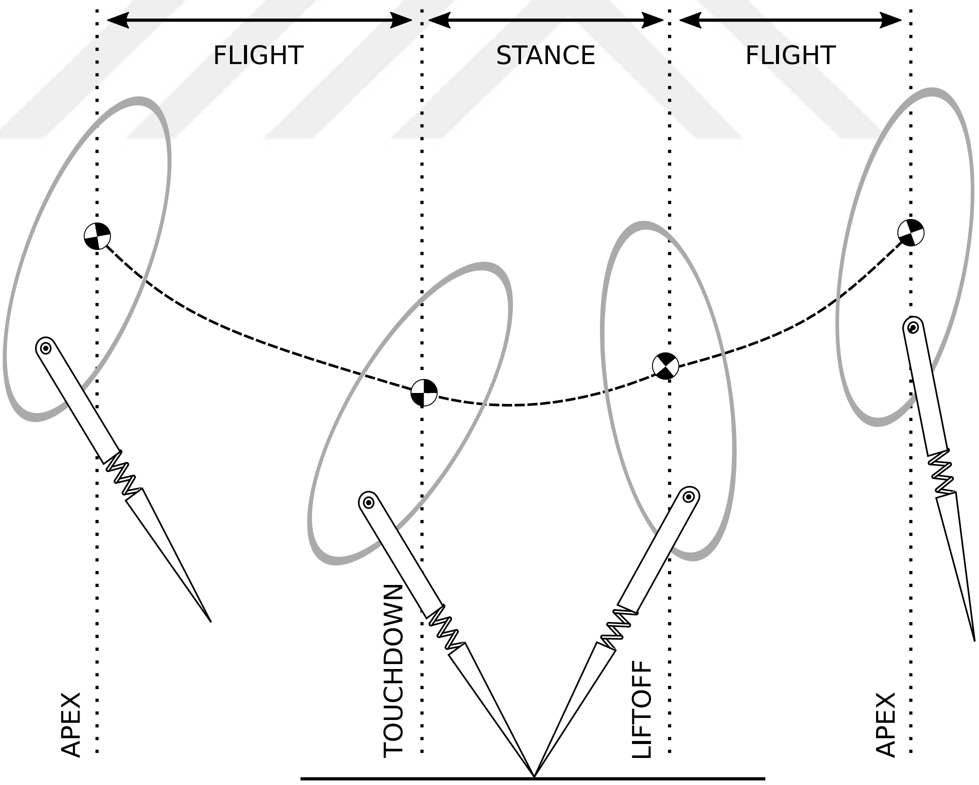

Figure 2.2: One step evolution of T-SLIP model

Table 2.1: Parameters and their definitions

Physical Parameters	Symbol	Value (unit)
Mass of the body	m	80 (kg)
Moment of inertia of the body	J	4.58 $(kg.m^2)$
Leg rest length	r_0	1 (m)
Distance between the hip and the CoM	d_{hip}	0.1 (m)
Spring coefficient	k	20 (kN/m)
Control Parameters	**Symbol**	**(Unit)**
Touchdown angle	α_{td}	(deg)
VPP distance	d_{vpp}	(m)
VPP angle	θ_{vpp}	(deg)

2.2 Virtual Pivot Point Concept

The Virtual Pivot Point is the point where all the ground reaction forces pass thorough. d_{vpp} and θ_{vpp} define the VPP location with respect to CoM (Fig. 2.1). If the only forcing element is spring force, the ground reaction forces can only pass through the hip of the T-SLIP model. To realize VPP, T-SLIP needs a hip torque. This torque depends on only the geometric relation between F_r and VPP. In other words, it behaves like a reflex. It instantaneously directs the ground reaction forces to VPP throughout the whole movement in the stance. We calculate the torque as

$$\tau_{vpp} = F_r \; r \; \frac{d_{hip} \; sin(\psi) + d_{vpp} \; sin(\psi + \theta_{vpp})}{r - d_{hip} \; cos(\psi) - d_{vpp} \; cos(\psi + \theta_{vpp})} \; . \tag{2.5}$$

Appendix B details the derivation and mathematical background of Eq. (2.5). When we adopt the VPP approach in the stance phase, two more gait level control parameters, (d_{vpp}, θ_{vpp}) (VPP distance and angle respectively), emerge in addition to the touchdown angle, α_{td}. In this context, the model proposes three gait level control parameters (Table 2.1). If there is no controller defined on the system, we set all the control parameters before executing the simulation.

2.3 Poincaré Return Map

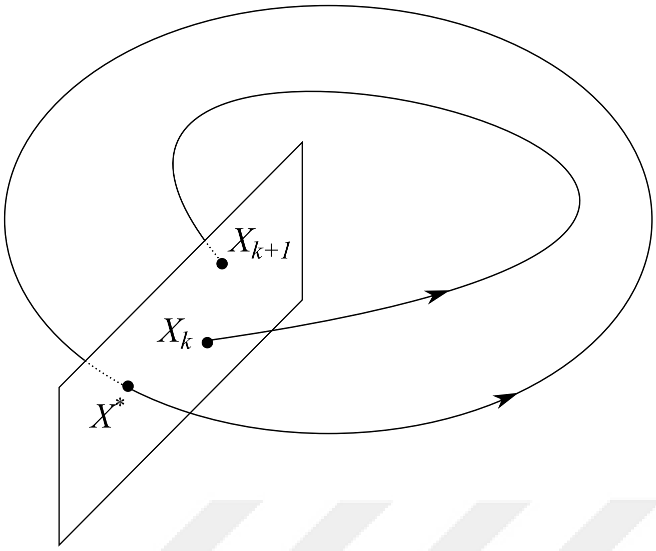

Figure 2.3: Illustration of a Poincaré map for a third order dynamical system

Poincaré return map is a powerful tool to analyze the running behavior because of its non-linear and periodic nature. This method intersects the periodic trajectories of a system whose state-space model is defined by n generalized coordinates with an $n-1$ dimensional hyperplane so that the periodic system's flow is expressed independently in time with $n-1$ coordinates. This hyper-plane crossing the trajectories is called the Poincaré Section. If the k^{th} intersection of the system state vector with this hyper-plane is called $\mathbf{X}_k$, defining the Poincaré Map as $F(\mathbf{X}_k) = \mathbf{X}_{k+1}$ express the relationship between the two consecutive intersections. All these definitions are represented in Fig. 2.3.

The periodic solutions of a system are the trajectories that always intersect the Poincaré Section from the same point, that is, $F(\mathbf{X}^*) = \mathbf{X}^*$ (see Fig. 2.3). This point, $\mathbf{X}^*$, on the Poincaré Section, is called a fixed-point. Existing fixed points of a model enables us to comment on the local stability of the around the fixed points. A first-order approximation of the Poincaré Map, F, around a fixed-point gives

$$\mathbf{X}_1 \approx F(\mathbf{X}^*) + A\,\Delta\mathbf{X}_0\,, \tag{2.6}$$

where $\Delta\mathbf{X}_0 = \mathbf{X}_0 - \mathbf{X}^*$ and we can define $\mathbf{X}_1 = \mathbf{X}^* + \Delta\mathbf{X}_1^*$. By replacing $\mathbf{X}_1$ and using the fact that $F(\mathbf{X}^*) = \mathbf{X}^*$, we can get

$$\Delta\mathbf{X}_1 \approx A\,\Delta\mathbf{X}_0 \ . \tag{2.7}$$

Eq. (2.7) maps the apex states around a fixed-point to next apex state. By looking the eigenvalues of A, we can comment on local stability of fixed-points. Let $|\lambda|_i$'s are the eigenvalues of A and define $|\lambda|_{max} = max||\lambda|_i|$. If $|\lambda|_{max} < 1$, any disturbance around the fixed-point dies out and results in asymptotically stable system. If $|\lambda|_{max} > 1$ the system is unstable. And finally, if $|\lambda|_{max} = 1$, the stability test is inclusive and we need further investigation. However, we do not focus this in this work. The matrix A is called Jacobian matrix, and throughout this dissertation we express it like this

$$A = \frac{\partial F}{\partial \mathbf{X}}(\mathbf{X}^*) \ . \tag{2.8}$$

In the VPP concept, we choose the hyperplane defined by

$$S_a = \{(\mathbf{q}, \dot{\mathbf{q}}) \mid \dot{z} = 0,\ [0,\ 0,\ 1] \cdot \mathbf{f}_s(\mathbf{q}) < 0\} \tag{2.9}$$

as the Poincaré Section. The conditions in Eq. (2.9) define the system's highest position on the vertical axis in the flight phase, i.e., apex state (see Fig. 2.2). Since the position of the system on the horizontal axis in the flight phase, x, does not affect dynamics, on this hyper-plane, the system state vector is defined $\mathbf{X}_k = [z,\ \dot{x},\ \theta,\ \dot{\theta}]^T \in S_a$ with four coordinate and the definition F becomes $F : S_a \rightarrow S_a$.

CHAPTER 3

THE ANALYSIS OF THE FIXED-POINTS OF THE VPP CONCEPT

In this chapter, we analyze the existence and the characteristics of the fixed points. We first explain the methodology of finding the fixed points. We then analyze the model's reachability/maneuverability by investigating the sub-manifolds composed of fixed positions inside the whole state-space. We also present the dependency of energetic efficiency on the control parameters and fixed point locations.

3.1 Identifiying The Fixed-Points of The VPP Concept

As we state in Section 2.1, there is no analytic solution of Eq. (2.2). We have to use numerical analysis methods to find the fixed-points of the VPP. We integrate the dynamics of the model using MATLAB "ode45" from apex to apex to compute Poincaré Map, F, as described in Section 2.3. Because of the errors come from numerical integration and round-off, finding the fixed points of the model becomes a search problem such that identifying the set $S_{\mathbf{X}^*} := \{\mathbf{X}_k \mid M > (\mathbf{X}_{k+1} - \mathbf{X}_k)^T W (\mathbf{X}_{k+1} - \mathbf{X}_k)\}$ gives the fixed points, where M is the threshold that determines which apex states are a fixed point, W is the weight matrix and $\mathbf{X}_{k+1} = F(\mathbf{X}_k)$. Note that the numerical integration tolerance, optimization algorithm tolerance, and M should be compatible.

To specify the set $S_{\mathbf{X}^*}$, we initialized "fminunc" algorithm of MATLAB from many different starting points that scan four-dimensional space, $\mathbf{X}_k = [z,\ \dot{x},\ \theta,\ \dot{\theta}]^T$. "fminunc" algorithm minimizes the function

$$\underset{\mathbf{X}_k}{argmin} \; \{\mathcal{H} = (\mathbf{X}_{k+1} - \mathbf{X}_k)^T W (\mathbf{X}_{k+1} - \mathbf{X}_k)\} \tag{3.1}$$

for each point. If a point that is found by "fminunc" algorithm satisfies the constraint

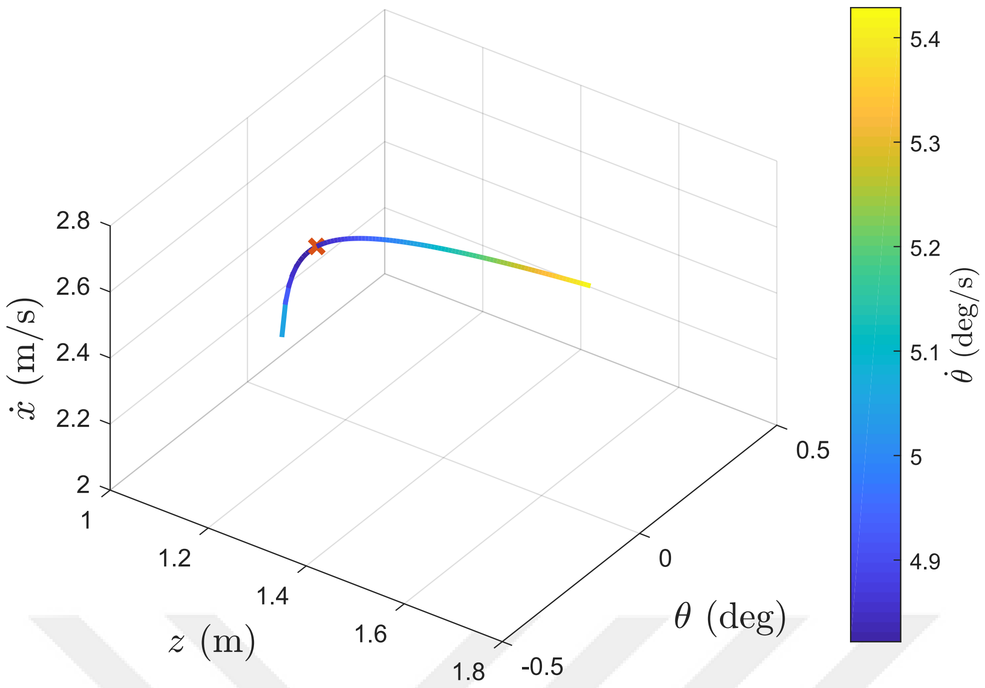

Figure 3.1: The fixed point distribution of VPP model when $\alpha_{td} = 105°$, $d_{vpp} = 0.1$ and $\theta_{vpp} = 0°$.

$M > (\mathbf{X}_{k+1} - \mathbf{X}_k)^T W(\mathbf{X}_{k+1} - \mathbf{X}_k)$, it becomes an element of the set $S_{\mathbf{X}^*}$.

Fig. 3.1 illustrates the fixed-points, $S_{\mathbf{X}^*}$, that are produced after executing the algorithm. For this particular example, we selected the control parameters as $\alpha_{td} = 105°$, $d_{vpp} = 0.1$ and $\theta_{vpp} = 0°$. Every point in Fig. 3.1 stands for a fixed-point. The continuum of the fixed-points forms a curve. Consequently, we can say that the fixed-points associated with the embedding the VPP concept on the T-SLIP model lies inside a one-dimensional manifold.

To strengthen our claim, we evaluate the cost function in Eq. (3.1) for a set of points on a cross-section from 4D apex state space. The apex states on the properly chosen cross-section that crosses the curve in Fig. 3.1 only one point should have only one minimum $\mathcal{H}$, if our claim is true. We choose the cross-section as the 3D space, which is defined by $z = 1.14m$. This space intersects the curve in Fig. 3.1 at the point shown by the red cross marker. We evaluate the cost function in Eq. (3.1) for points that scans this 3D space. Fig. 3.2 illustrates the corresponding results. As expected, we have a single minimum on this space, which is the intersection of the fixed-point

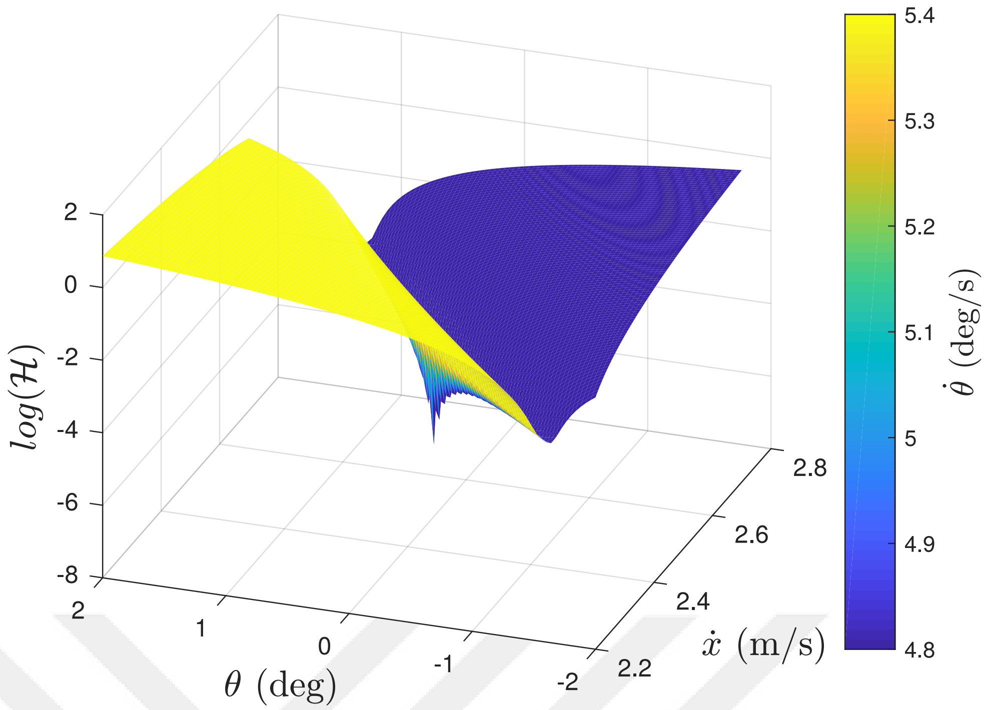

Figure 3.2: $\mathcal{H}$ of the apex states on the cross-section of $z = 1.14m$ plane and Fig. 3.1

manifold and $z = 1.14m$ in 3D space. In this context, we can conclude that our claim is valid when the control parameters are $\alpha_{td} = 105°$, $d_{vpp} = 0.1$ and $\theta_{vpp} = 0°$. We validated that the claim still holds when we select the control parameters from the following range by repeating the same set of simulations and analysis

$$91° < \alpha_{td} < 120°, \tag{3.2a}$$

$$0.1m < d_{vpp} < 1m, \tag{3.2b}$$

$$-2° < \theta_{vpp} < 2° \; . \tag{3.2c}$$

Fig. 3.3 shows one example of a periodic solution trajectory associated with a fixed point that belongs to the red cross marker on Fig. 3.1. One can see that all the states return to their original locations in the next apex instant, which comes from the definition of the fixed point. Fig. 3.4 illustrates the power and torque requirements of the corresponding periodic solution on Fig. 3.3. Since the system's initial and final total energy are equal, the net actuation work of the hip torque is zero. We can observe this result on Fig. 3.4, such that positive and negative power cancel each other. We also illustrate the $\tau - \psi$ graph which provides a similar outcome to the results in [47]. This torque profile could enable us to use elastic elements to implement Eq. (2.5) in

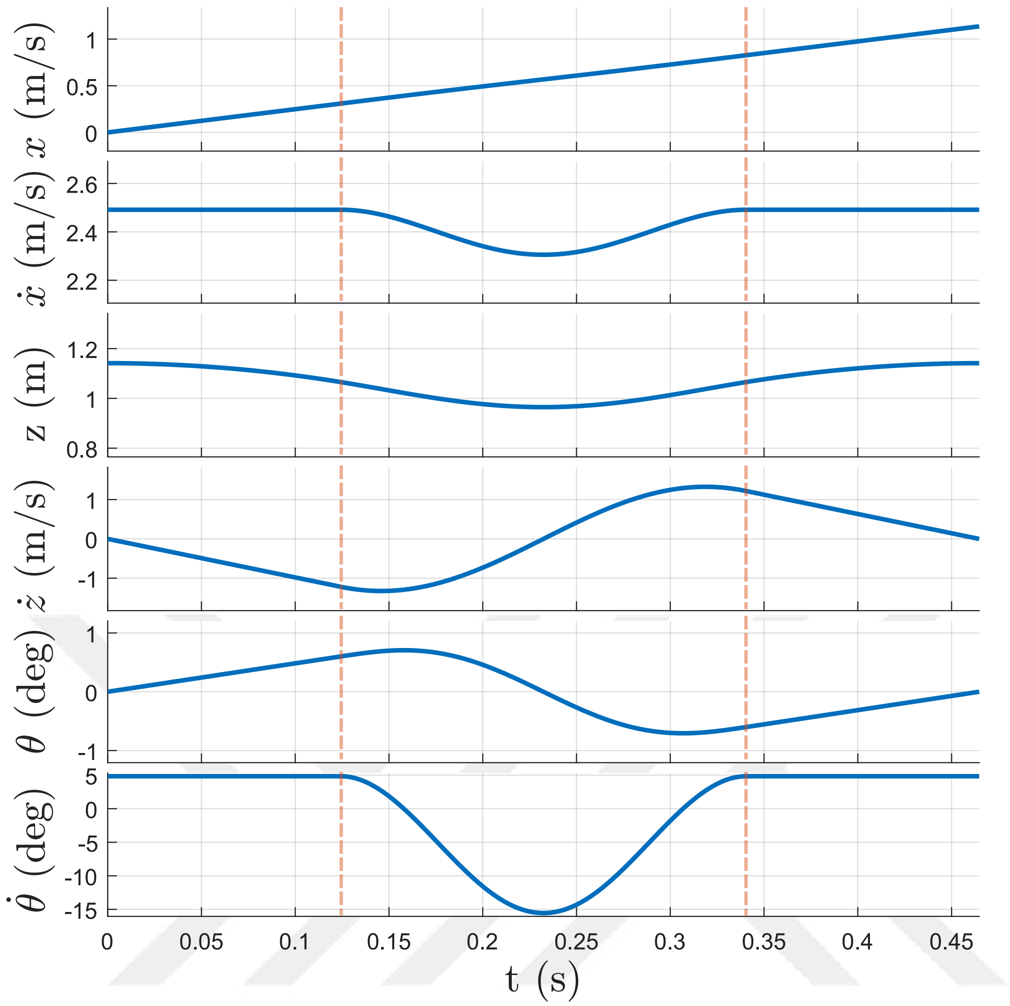

Figure 3.3: The state evaluation of T-SLIP model under VPP concept from apex to apex. The vertical dashed lines represent the touchdown and lift-off instances.

the future. There are various studies in the literature on this topic [47, 48, 49].

3.2 The Characteristics of The Fixed-Points

We performed systematic simulations for different values of control parameters to characterize and analyze fixed-points and associated periodic solution properties. In these simulations, we particularly choose d_{vpp} and θ_{vpp} from

$$\{0.1m,\ 0.4m,\ 1m\}, \tag{3.3a}$$

$$\{-2^{\circ},\ 0^{\circ},\ 2^{\circ}\} \tag{3.3b}$$

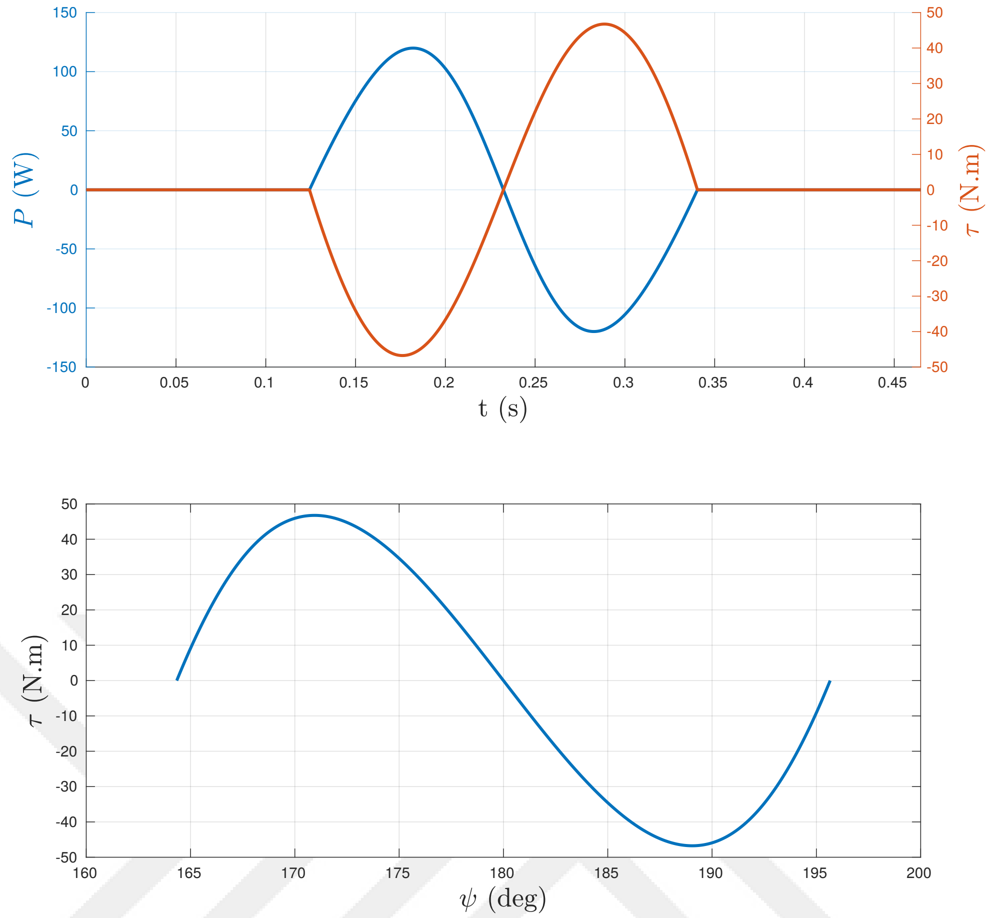

Figure 3.4: Top graph shows the power and the torque applied by the hip torque in blue and red, respectively. The below figure shows how behaves the hip torque with respect to body-leg angle, ψ.

respectively, and for every pair of d_{vpp}-θ_{vpp} we sweep α_{td} from $91°$ to $120°$. We run the optimization algorithm for every set of control parameters (α_{td}-d_{vpp}-θ_{vpp}) and find the associated fixed-points.

We apply Spearman's Rank Correlation to the fixed-point that comes from the collection of control parameters. The correlation analysis indicates the dependency of the elements of the apex state on the control parameters. Table 3.1 presents the associated results. There are four core points that one conclude from Table 3.1:

- θ mostly depends on θ_{vpp}, and the other control parameters have little effect on θ,
- θ_{vpp} does not affect the states significantly other than θ,

Table 3.1: Spearman's rank correlation between control parameters and fixed-points

Control Parameters \ Apex State	z		$\dot{x}$		θ		$\dot{\theta}$	
	ρ	p	ρ	p	ρ	p	ρ	p
α_{td}	-0.151	0	0.933	0	-0.042	0.008	0.327	0
d_{vpp}	-0.117	0	-0.489	0	0.028	0.074	0.613	0
θ_{vpp}	-0.024	0.051	0.036	0.003	-0.980	0	-0.017	0.165

- Based on the previous two results, we can say that θ can be selected without affecting other states,
- α_{td} is strongly correlated with $\dot{x}$. We discuss this result later.

Spearman's Rank Correlation allows us to roughly see the relationship between control parameters and fixed points. In the following figures, we will analyze the effect of the control parameters more comprehensively. In this dissertation, we only show plots about two different cases in which:

- **Case I**: θ_{vpp} is held constant, its value is $0°$, d_{vpp} is chosen from Eq. (3.3a) and every pair of d_{vpp}-θ_{vpp} we sweep α_{td} from $91°$ to $120°$,
- **Case II**: d_{vpp} is held constant, its value is $0.1m$, θ_{vpp} is chosen from Eq. (3.3b) and every pair of d_{vpp}-θ_{vpp} we sweep α_{td} from $91°$ to $120°$.

Although we express the characteristics of the fixed-points for these two cases, we verified that the results could be generalized for other pairs of $d_{vpp} - \theta_{vpp}$ that given in Eq. (3.3a) and Eq. (3.3b).

In this section, the color codes on the fixed-point manifold illustrations represent some of the fixed-point characteristics. In each figure, we choose three out of four-element from the apex state variables, $\mathbf{X}_k$ for representation. The results in Table 3.1 enable us to pick which coordinate axis to show. If θ_{vpp} is constant (Case I), we only show z, $\dot{x}$ and $\dot{\theta}$ as coordinate axes since θ is mostly influenced by θ_{vpp}. Otherwise,

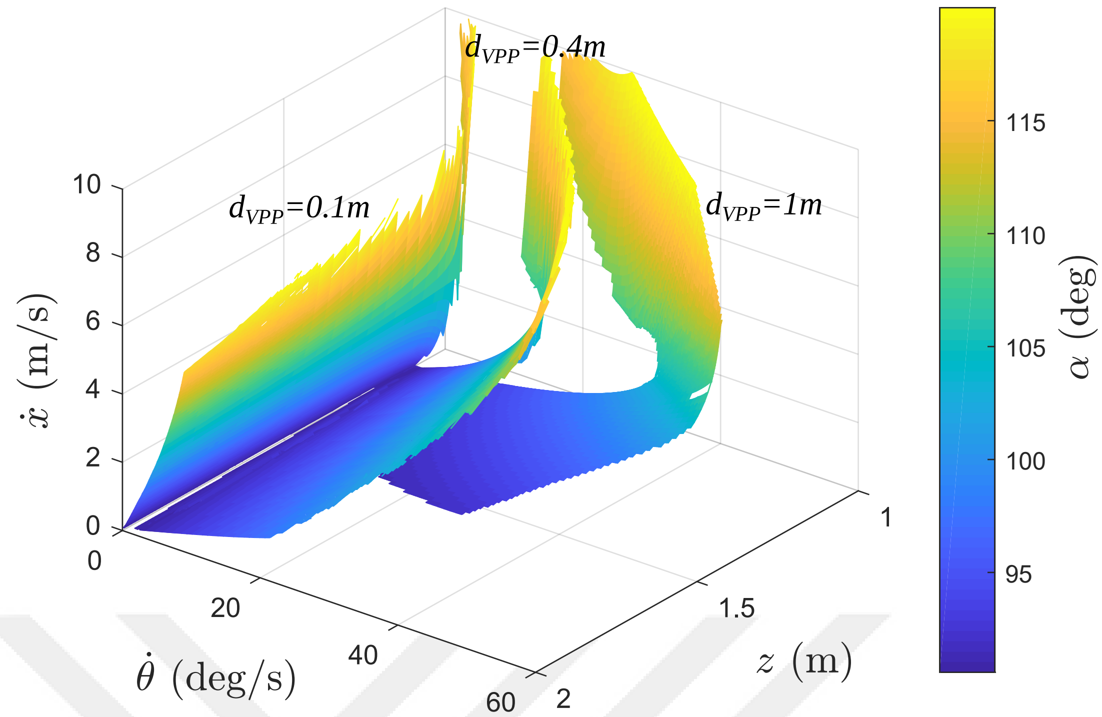

Figure 3.5: The fixed-point distribution for different d_{vpp} values when $\theta_{vpp} = 0°$.

we replace $\dot{x}$ with θ since the correlation between $\dot{x}$ and θ_{vpp} is significantly less (Case II).

Fig. 3.5 and Fig. 3.6 shows distribution and coverage of the fixed-points inside the whole state-space by changing control parameters. Broader coverage enables increased maneuverability, i.e., the system can run at different heights, speeds, pitch angles, and pitch rates. Also, existing fixed-points on many different states enable us to design a controller for that particular state.

The results from Fig. 3.5 and Fig. 3.6 can be summarized as follows:

- With the increasing α_{td}, $\dot{x}$ increases while the shape of curve in Fig. 3.1 is preserved. This result also can be seen on Table 3.1. α_{td} has low correlation with the elements of the apex state except $\dot{x}$. There are intuitive controllers that control touchdown leg angle, α_{td} to control horizontal speed [14, 17, 50, 51]. These controllers support this result.

- With the increasing d_{vpp}, the system's $\dot{\theta}$ increases,

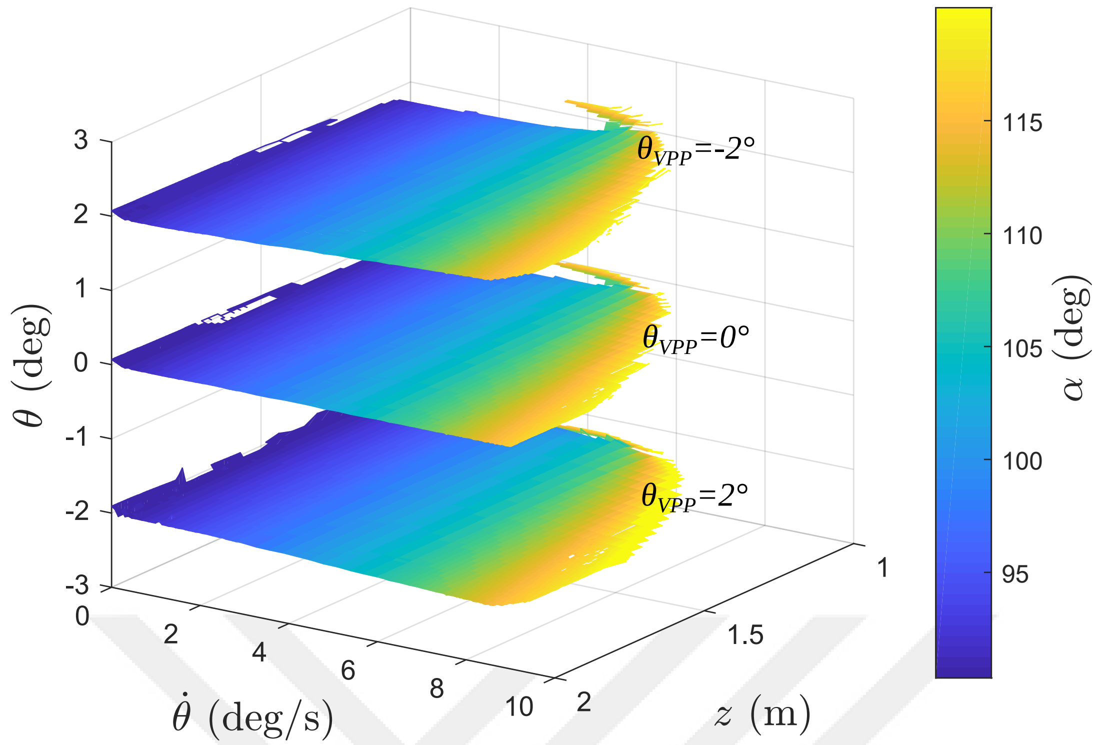

Figure 3.6: The fixed-point distribution for different θ_{vpp} values when $d_{vpp} = 0.1m$.

- θ_{vpp} and θ is roughly inversely proportional.

Note that, since θ of the fixed-points does not change with d_{vpp} (Table 3.1), the surfaces on Fig. 3.5 has the same θ which is 0 and since θ_{vpp} does not affect the states except θ, the surfaces on Fig. 3.6 has the same distribution on Fig. 3.5 when $d_{vpp} = 0.1m$.

The cost of transport, $\mathcal{C}$, is a dimensionless quantity that measures the energetic efficiency of locomotion. One can obtain the cost of transport by dividing the energy applied to the system by path traveled, system mass, and gravitational acceleration. However, in simplified systems like T-SLIP, the net energy applied to the system is 0 on the periodic solutions. So we integrate absolute power over time to calculate the energy as in [52, 53],

$$\mathcal{C} = \frac{1}{mgd} \int_{t_0}^{t_1} |P(t)| dt \,. \tag{3.4}$$

We use this cost of transport, $\mathcal{C}$, to compare the fixed-points of the VPP to each other. In a real system $\mathcal{C}$ can be lower as stated in [52]. Since the VPP concept enables us to use passive elastic elements to implement/approximate the necessary

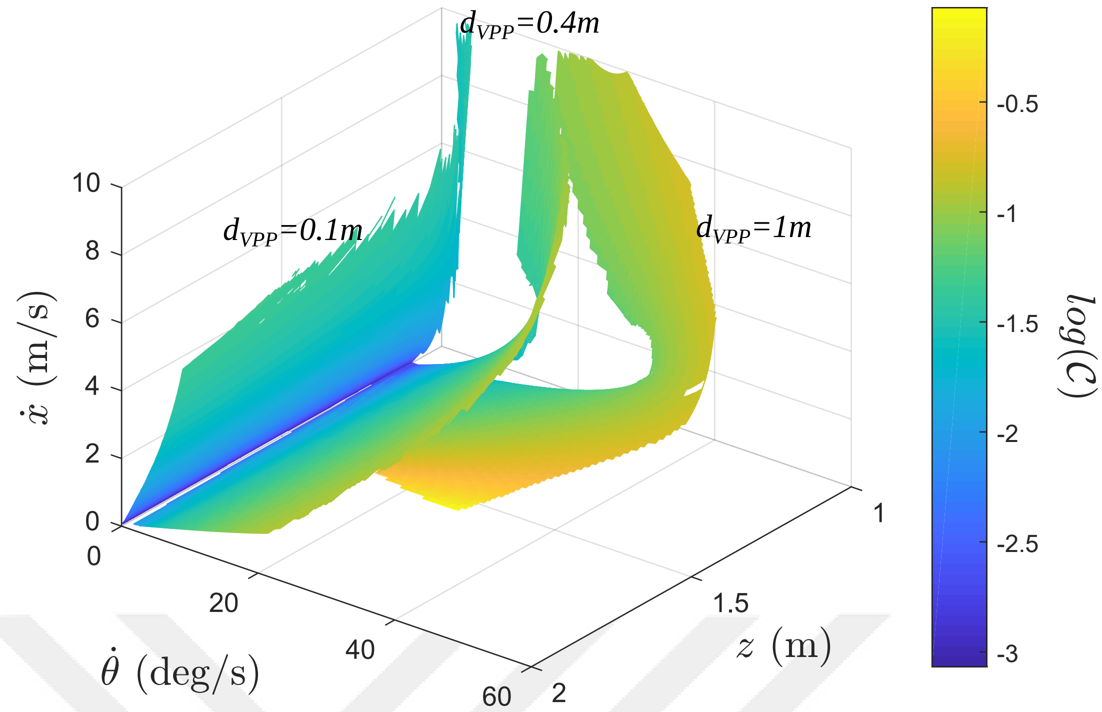

Figure 3.7: Cost of transport, $\mathcal{C}$, of the fixed points given in Fig. 3.5

torque,[47, 48, 49], or the efficient motor drivers, [54], can store the negative work at the batteries.

The results from Fig. 3.7 and Fig. 3.8 can be summarized as follows:

- The cost of transport does not change with the apex height. Also, on the 1-manifold, while apex height changing, the change in the speed, $\dot{x}$, and the pitch rate, $\dot{\theta}$, remain limited, and the pitch, θ, does not change at all. So, one can select the desired apex height without losing efficiency and affecting other states significantly.
- Low speed, $\dot{x}$ results in a better cost of transport
- When the body is perpendicular to the ground, $\theta = 0°$, the system has the best cost of transport.
- Low values of pitch rate, $\dot{\theta}$, gives a better cost of transport.

Finally, we analyzed the stability of the fixed points. We evaluated linearized system matrix in Eq. (3.5) for every fixed-point in Fig. 3.5 and Fig. 3.6. As in the case of

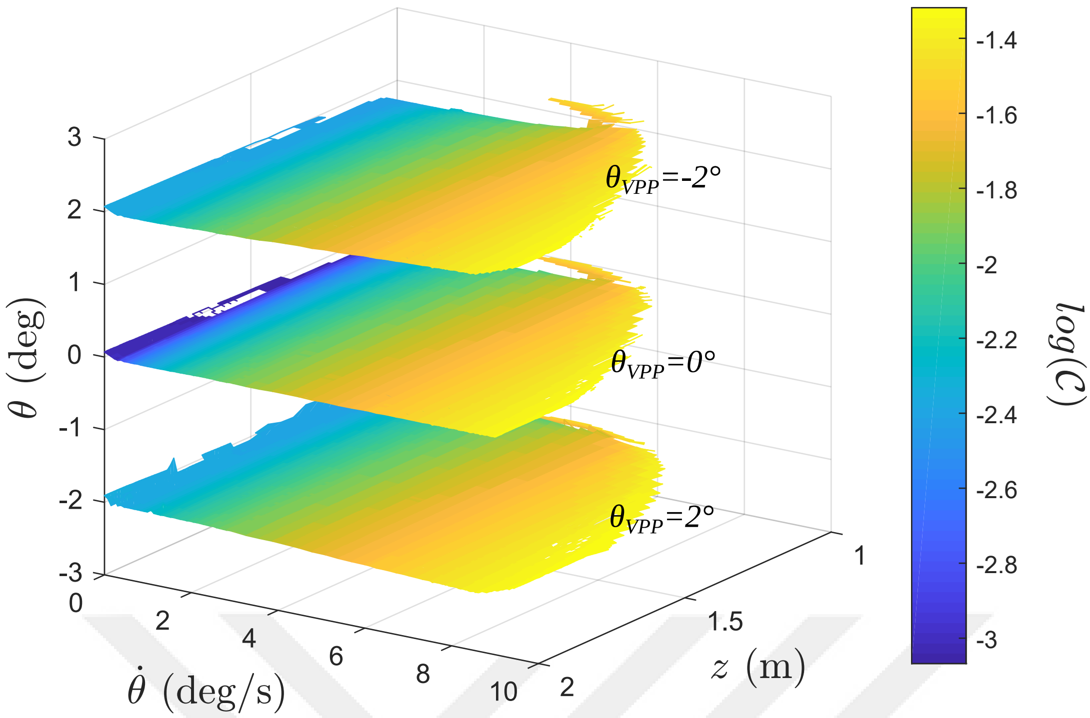

Figure 3.8: Cost of transport, $\mathcal{C}$, of the fixed points given in Fig. 3.6

finding the fixed-points, we need to adopt numerical methods to compute A. We use central difference method of order $\mathcal{O}(h^4)$ to approximate the linearized system matrix around the fixed point:

$$A = \frac{\partial F}{\partial \mathbf{X}}(\mathbf{X}^*) \approx \frac{-F(\mathbf{X}+2\mathbf{h}) + 8F(\mathbf{X}+\mathbf{h}) - 8F(\mathbf{X}-\mathbf{h}) + F(\mathbf{X}-2\mathbf{h})}{12\mathbf{h}}, \tag{3.5}$$

where $\mathbf{h}$ is the step size. Selection appropriate h is a challenging problem. Larger values of h do not yield a good approximation since it captures higher-order non-linear components. On the other hand, small values of h that are comparable with machine precision and accuracy results in numerical errors in calculations. The overcome this difficulty, we use the algorithm presented in [55]. This algorithm enables us to pick the unique step size for each fixed-point in every direction. The algorithm details are on Algorithm 1 where, $\mathbf{D}(i)$'s represent each column of A matrix, $\mathbf{h}_i$'s are unit vector in 4D, h_{max} is the maximum step size, and tol is the tolerance value that step size does not go beyond it, and it should be compatible with the numeric integration tolerance and machine precision.

The maximum of absolute value of eigenvalues, $|\lambda|_{max}$, of A for every fixed-point

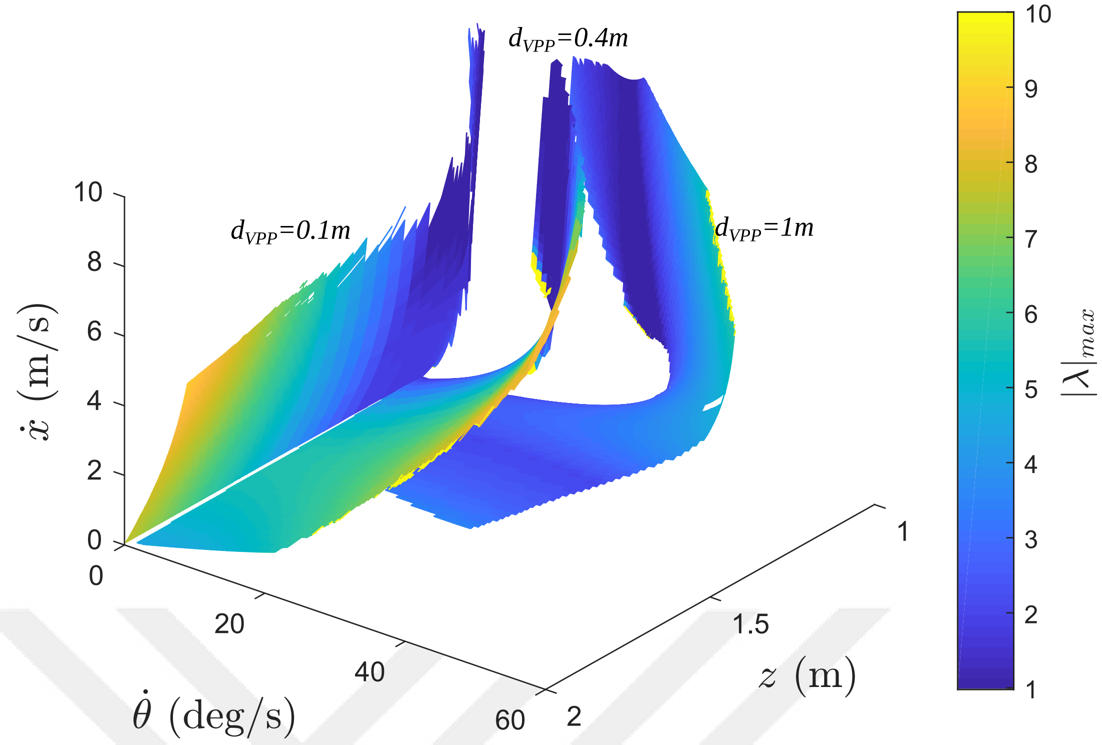

Figure 3.9: Maximum absolute eigenvalues, $|\lambda|_{max}$, of the Jacobi matrix calculated for the fixed-points given in Fig. 3.5.

is plotted on Fig. 3.9 and Fig. 3.10. As seen, most of the fixed-points are unstable. For the rest, the stability test is inclusive. This result is compatible with a one-dimensional fixed-point manifold. If the perturbation pushes the model another point on the manifold, the perturbation will be preserved. The eigenvalue that corresponds to the eigenvector in the direction of the manifold is always 1. We can conclude that the stability test for the fixed-points of the VPP concept on the T-SLIP model results in either inclusive or unstable behavior. Therefore, to run on the desired trajectory, a controller action is needed. We will give the details on the controllers in Chapter 4.

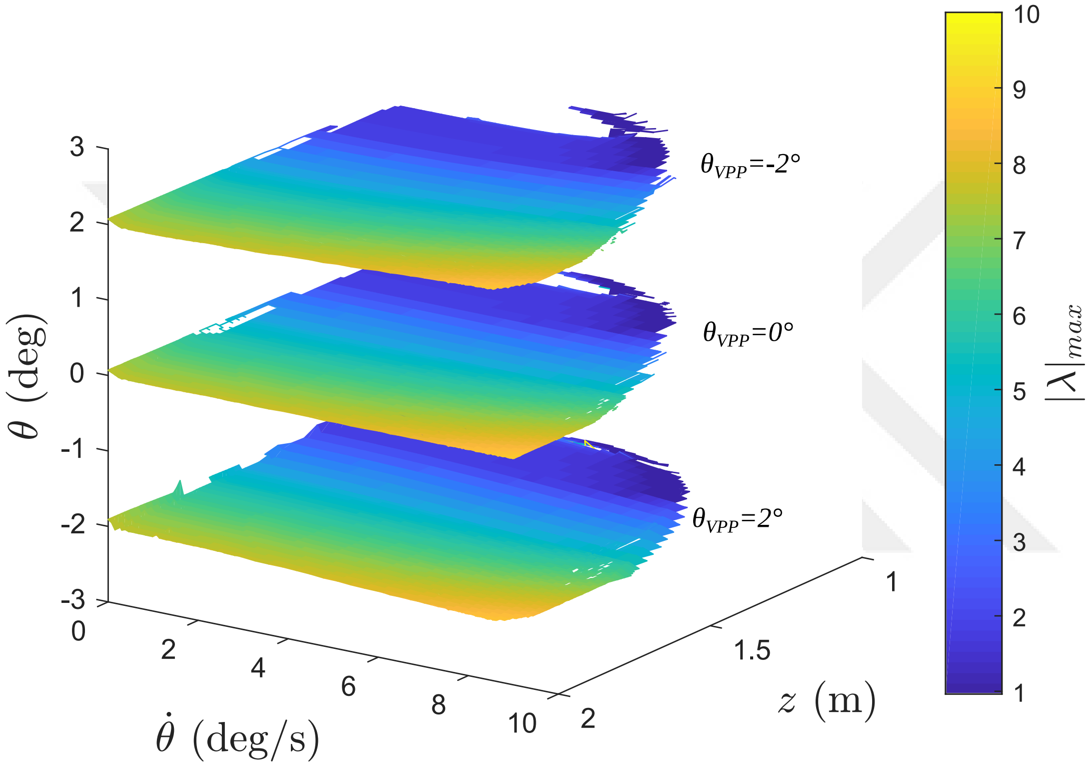

Figure 3.10: Maximum absolute eigenvalues, $|\lambda|_{max}$, of the Jacobi matrix calculated for the fixed-points given in Fig. 3.6.

Algorithm 1 Jacobian Matrix Calculation

procedure CENTRAL DIFFERENCE(F, h_{max}, tol)

    for $i = 1; i \leq 4; i++$ **do**

        $\mathbf{h}_i = h_{max}\, \mathbf{h}_i$;

        $\mathbf{D}(1) = \frac{-F(\mathbf{X}+2\mathbf{h}_i)+8F(\mathbf{X}+\mathbf{h}_i)-8F(\mathbf{X}-\mathbf{h}_i)+F(\mathbf{X}-2\mathbf{h}_i)}{12\mathbf{h}_i}$;

        $\mathbf{h}_i = \mathbf{h}_i/2$;

        $\mathbf{D}(2) = \frac{-F(\mathbf{X}+2\mathbf{h}_i)+8F(\mathbf{X}+\mathbf{h}_i)-8F(\mathbf{X}-\mathbf{h}_i)+F(\mathbf{X}-2\mathbf{h}_i)}{12\mathbf{h}_i}$;

        $j = 3$;

        while true **do**

            $\mathbf{D}(j) = \frac{-F(\mathbf{X}+2\mathbf{h}_i)+8F(\mathbf{X}+\mathbf{h}_i)-8F(\mathbf{X}-\mathbf{h}_i)+F(\mathbf{X}-2\mathbf{h}_i)}{12\mathbf{h}_i}$;

            if $|\mathbf{D}(j) - \mathbf{D}(j-1) \geq |\mathbf{D}(j-1) - \mathbf{D}(j-2)||$ **then**

                $A(:, i) = D(j-1)$;

                break;

            else if $|\mathbf{D}(j) - \mathbf{D}(j-1) < tol$ **then**;

                $A(:, i) = D(j)$;

                break

            else

                $\mathbf{h}_i = \mathbf{h}_i/2$;

            end if

            $j = j + 1$;

        end while

    end for

end procedure

CHAPTER 4

THE GAIT CONTROLLERS

The analysis and results presented in Chapter 3 show that fixed-points are not passively stable (when we keep the gait level controllers constant throughout locomotion). In that respect, we need to design a (feedback) controller to stabilize these fixed-points. In addition to the local stability of fixed points characterized by the linearized system's eigenvalues, we also need to create a relatively large region of attraction around the limit-cycle to obtain a robust locomotion behavior. In this context, we design different feedback controllers for the proposed system and evaluate their performances in terms of linear (eigenvalues) and non-linear stability (basins-of-attraction). In this section, we will explain the mathematical background of the designed controllers. In the subsequent section, we will present closed-loop simulation results and perform a comparative analysis between different types of controllers.

4.1 Mathematical Background

The core aim of the controller design is to find a feedback policy such that T-SLIP trajectories converge to the periodic solutions of VPP. It may be possible to achieve this goal via continuous-time feedback controllers that continuously track the error between the actual and desired trajectories and update control inputs based on these error functions [56]. However, due to the highly non-linear and hybrid structure of locomotion, designing such a controller is very challenging. For example, the T-SLIP model is technically totally uncontrollable/unreachable. The alternative and common approach in the legged locomotion field is to develop discrete-time gait level controllers that only "update" the control actions at the selected Poincare sections similar to the zero-order hold operation in digital control systems [57, 58, 26, 59, 60]. This approach produced successful practical and theoretical results in legged locomotion, and thus we also adopt this methodology in this thesis. Linearization of the Poincare Map around a fixed point yields a linear discrete-time system that approximates the evolution of states from one intersection to the next. The advantage of this approach is that conventional discrete-time controllers can compute the "necessary" control actions to stabilize the system around the fixed point. As a discrete-time controller, we prefer to use LQR because of its inherent robustness against model uncertainties [61] as well as relatively simple design and implementation processes. Based on the control action, the Poincare Map becomes

$$F_{cont}(\mathbf{X}_k, \mathbf{u}_k) \; = \; \mathbf{X}_{k+1} \; . \tag{4.1}$$

Then the linearization of F_{cont} around a fixed point gives us,

$$\Delta\mathbf{X}_{k+1} = A \; \Delta\mathbf{X}_k + B \; \Delta\mathbf{u}_k \; , \tag{4.2}$$

where $A = \frac{\partial F_{cont}}{\partial \mathbf{X}}(\mathbf{X}^*, \mathbf{u}^*)$, $B = \frac{\partial F_{cont}}{\partial \mathbf{X}}(\mathbf{u}^*)$, $\Delta\mathbf{X}_k = \mathbf{X}_k - \mathbf{X}^*$, $\Delta\mathbf{u}_k = \mathbf{u}_k - \mathbf{u}^*$.

To control the discrete time system given in Eq. (4.2), we use infinite-horizon LQR controller, [62]. The cost function is defined as follows

$$J = \sum_{k=0}^{\infty}(\mathbf{X}_k^T Q \mathbf{X}_k + \mathbf{u}_k^T R \mathbf{u}_k) \; , \tag{4.3}$$

where Q and R are positive definite matrices. The optimal state feedback, K, which minimizes Eq. (4.3), is

$$K = (R + B^T P B)^{-1} B^T P A \; , \tag{4.4}$$

where P is the solution of the following discrete Riccati Algebraic Equation

$$P = Q + A^T (P - P B_S (B^T P B + R)^{-1} B^T P) A \; . \tag{4.5}$$

Finally, $\mathbf{u}_k$ in Eq. (4.2) is calculated as follows

$$\mathbf{u}_k = -K \; \Delta\mathbf{X}_k \; . \tag{4.6}$$

As a controller input, several options are available for templates like T-SLIP. Touch-down leg angle, α_{td}, is the most natural and ubiquitous controller input [63, 64, 65].

In order inject (and absorb) energy into (and from) templates, variable/active damping coefficients and/or spring coefficients [66, 67], precompression of the leg [17], series-elastic radial force actuation [68], and direct hip torque actuation are some of the other preferred input types. Therefore, one can design a controller using different controller inputs. At this stage, if we have some flexibility in choosing the system's inputs, what should be decision criteria?

Typical problems that legged systems encounter are model uncertainties, sensory noise, and environmental disturbances. Designs that offer more robustness can potentially handle these difficulties more effectively. So, we can choose appropriate control inputs from the set we mentioned earlier to achieve this. However, we first need to measure robustness systematically for each design, and there are studies on this topic in the literature. Heim et al. [69] and Zaytsev et al. [70] quantify the robustness in locomotive behaviors using viability theorem. Although these approaches offer promising results for the low-dimensional template models, they are not directly scalable to the T-SLIP model. To the best of our knowledge, testing & evaluating control inputs for T-SLIP like models to guide the controller design process is currently an open problem.

Another criterion could be selecting control inputs that offer better embedding into real systems. There are several works on how to change effectively the energy of the SLIP [71, 66, 67, 17]. However, unlike SLIP, T-SLIP has an actuation on the hip. We have more flexibility to inject energy to model or absorb from it. So, we do not consider this criterion in this thesis.

Eventually, in this dissertation, we focus on two different sets of controller inputs that are morphologically different from each other. The first one is the control scheme called Virtual Pendulum Based Posture Control (VPPC) [46]. In this control scheme, Sharbafi et al. use VPP parameters and α_{td} to design a feedback controller for the model. In addition to this, we introduced a new control scheme, called Parameterized Torque Control (PTC). PTC is technically an additive torque control policy built on top of $\tau_v pp$ along with α_{td} control. We provide the details of the controller schemes in the following sections.

4.2 Gait Controllers

4.2.1 The Virtual Pendulum Based Posture Control

In this section, we will briefly summarize the VPCC control scheme introduced by Sharbafi et al. [46] to control the vertical hopping (only) motion of the T-SLIP template. The proposed study also provides experimental verification of the controller on a physical robot platform that inevitably includes leg mass, inertia, and damping. In this control scheme, the adopted set of controllers are

$$\mathbf{u}_k = \begin{bmatrix} \alpha_{td} \\ d_{vpp} \\ \theta_{vpp} \end{bmatrix} . \tag{4.7}$$

In the exiting study, a velocity based leg adjustment function computes the necessary α_{td} and an LQR regulator computes d_{vpp} and θ_{vpp} [46]. In our work, we design an LQR controller to calculate all the elements of the control input set, $\mathbf{u}_k$. As we disussed previously, linerazition of the Poincare Map, Eq. (4.1), for Eq. (4.7) yields a discrete time dynamical system in the form of Eq. (4.2). Then we calculate the “optimal” state feedback given in Eq. (4.4). which then computes the input actions given in Eq. (4.6).

This set of control actions ensures that the model’s dynamic behavior satisfies the VPP concept’s constraints during both transients and periodic solutions. In other words, ground reaction forces always pass through to the VPP no matter what the computed control action is. The controller attempts to stabilize the system by changing the VPP location per cycle/step.

Researchers developed the VPP scheme inspired by the average steady-state locomotion behavior in animals. However, there might not bet a fixed VPP location when animals change their running speed or height or recover from external perturbations. In this study, we propose an additive torque on top of τ_{vpp} instead of Virtual Pendulum Based Posture Control.

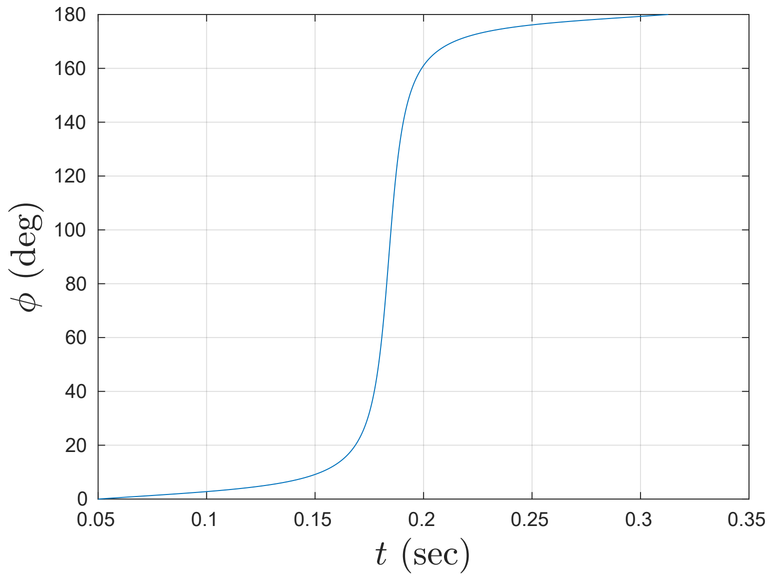

Figure 4.1: Phase, ϕ, of T-SLIP model from TD to LO.

4.2.2 The Parameterized Torque Control

The core idea of the proposed control scheme is to utilize the torque actuation at the hip in the closed-loop control policy to stabilize the fixed points. We call this controller as Parameterized Torque Control (PTC). PTC generates an additive torque action on top of τ_{vpp} in the form of

$$\tau = \tau_{vpp} + \tau_{cont} \ . \tag{4.8}$$

We parameterize τ_{cont} as

$$\tau_{cont}(\phi) = a_0 + a_1\ \phi + a_2\ \phi^2\ , \tag{4.9}$$

where ϕ is the "phase" of the system in the stance phase. We define ϕ as

$$\phi = atan2(r_{td} - r, -\dot{r})\ . \tag{4.10}$$

Time-based τ_{cont} can potentially create some problems due to phase resetting phenomena, which is inevitable for non-clock driven rhythmic dynamical systems [72, 73]. We linearize the input-driven system around a fixed-point, and then the state-feedback rule computes the coefficients of τ_{cont} using this linearization. The linearization assumes that stance time is constant, and τ_{cont} is defined for that particular stance phase. However, the disturbances can change stance time, early or late lift-off can happen. τ_{cont} should be scalable according to the stance phase. This phase definition enables us to apply torque depending on the system's state so that linearization works on the broader region. The evaluation of the phase variable from touchdown to lift-off is in Fig. 4.1.

The resulting the set of controller input becomes

$$\mathbf{u}_k = \begin{bmatrix} \alpha_{td} \\ a_0 \\ a_1 \\ a_2 \end{bmatrix}. \tag{4.11}$$

As in the Virtual Pendulum Based Posture Control, linearization of Poincare Map, Eq. (4.1), for Eq. (4.7) yields a discrete-time system in the form of Eq. (4.2). We then calculate the optimal state feedback given in Eq. (4.4) and the input given in Eq. (4.6). Unlike VPCC, this set of control relaxes the constraint on the ground reaction forces during transients. However, it comes with the cost of additional sensory information because of the phase's measurement, ϕ that depends on the system's variables.

CHAPTER 5

PERFORMANCE OF THE GAIT CONTROLLERS

In this chapter, we present our systematic simulation results where we test and compare the performances of controllers detailed in Chapter 4. While VPPC has three control inputs, PTC has four control inputs. Since the difference in the control degrees of freedom can be unfair when comparing both controllers, we modify PTC to have three control inputs by eliminating one of the torque profile coefficients, i.e., $a_2 = 0$ in Eq. (4.11). We call this new controller PTC-L. We perform simulation tests with these three controllers for four different fixed-points. In these simulations, we choose Q and R matrices in Eq. (4.3) as $Q = I_{4x4}$, $R = 0.01 \cdot I_{4x4}$ for PTC and $R = 0.01 \cdot I_{3x3}$ for VPPC and PTC-L.

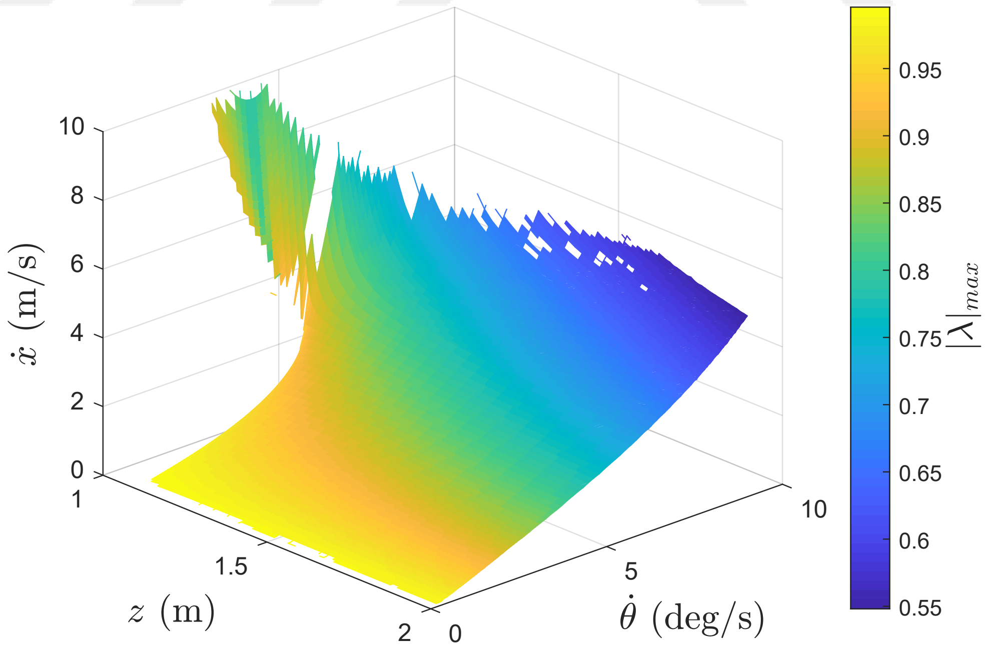

Figure 5.1: Maximum absolute eigenvalues, $|\lambda|_{max}$, of the Jacobi matrix calculated for the fixed-points given in Fig. 3.6 with VPPC, when $d_{vpp} = 0.1m$ and $\theta_{vpp} = 0°$.

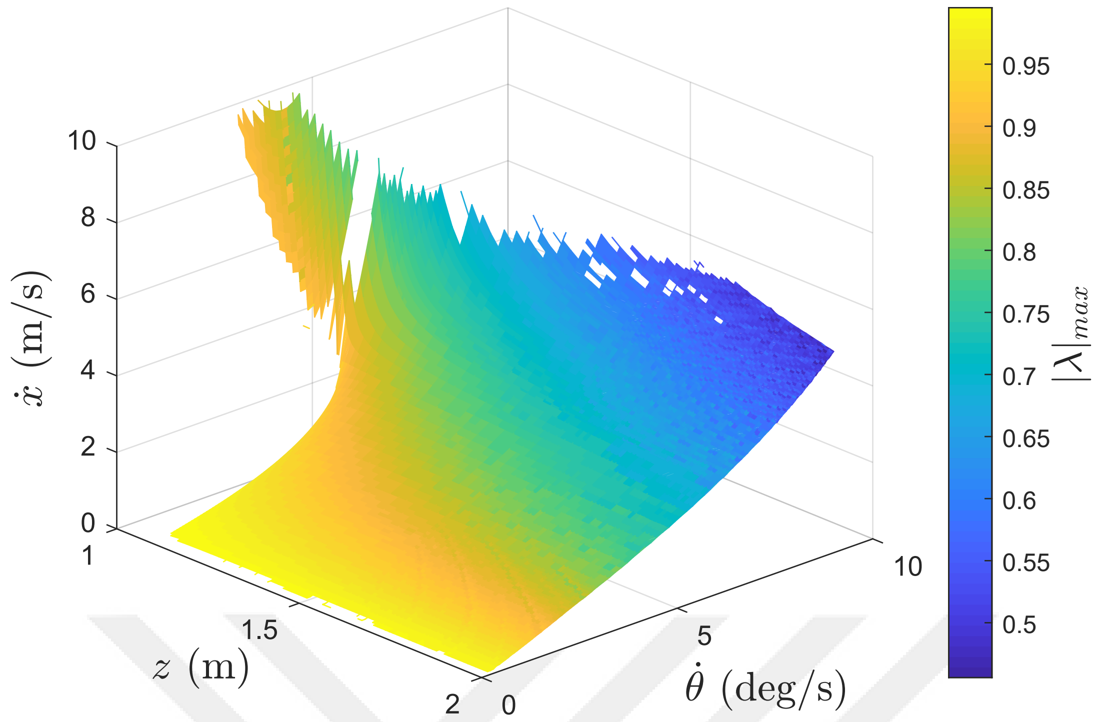

Figure 5.2: Maximum absolute eigenvalues, $|\lambda|_{max}$, of the Jacobi matrix calculated for the fixed-points given in Fig. 3.6 with PTC, when $d_{vpp} = 0.1m$ and $\theta_{vpp} = 0°$.

First of all, we need to verify and test local linear stability. Thus, we compute the eigenvalues of the closed-loop (when controllers are in action) linearized dynamics around the selected fixed-points. For a (locally) stable behavior, the linearized system matrix's eigenvalues have to stay inside the unit circle in the complex plane strictly, i.e., $|\lambda|_{max} < 1$ For all the fixed-points that have $d_{vpp} = 0.1m$ and $\theta_{vpp} = 0°$ in Fig. 3.6, we generate the controllers and evaluate the Jacobian matrices under the controller action. Fig. 5.1, Fig. 5.2 and Fig. 5.3 illustrates these results, As shown, all three controllers can successfully stabilize the template plant and moreover the controllers exhibit similar performance. One can observe a noticeable difference in the minimum values of $|\lambda|_{max}$, where PTC can provide lower (i.e., faster) $|\lambda|_{max}$ compared to the other two control policies.

We additionally compare the performances of these controllers based on their basins of attraction and settling time performances. We performed simulations for four different fixed-points, which are on Table 5.1, due to the high computational demand of the test processes. We choose these fixed-points such that they are distant from each

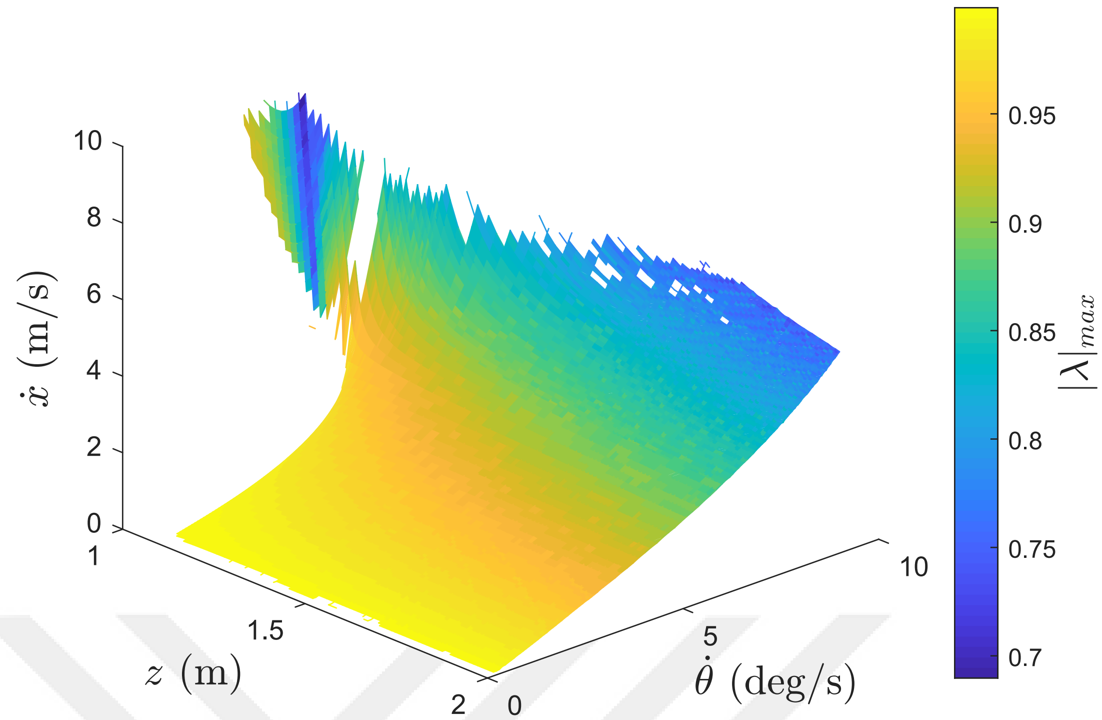

Figure 5.3: Maximum absolute eigenvalues, $|\lambda|_{max}$, of the Jacobi matrix calculated for the fixed-points given in Fig. 3.6 with PTC-L, when $d_{vpp} = 0.1m$ and $\theta_{vpp} = 0°$.

other and have significantly different control parameter values. To determine the basin of attraction for each fixed-point, we perform batch simulations in the fixed-points neighborhood. In particular, we start simulations from a set of initial points $\mathbf{X}_0 = \mathbf{X}^* + [\Delta z,\ \Delta\dot{x},\ \Delta\theta, \Delta\dot{\theta}]^T$ where

$$-0.2 \leq \Delta z \leq 0.2 \tag{5.1}$$

$$-1 \leq \Delta\dot{x} \leq 1 \tag{5.2}$$

$$-30° \leq \Delta\theta \leq 30° \tag{5.3}$$

$$-60° \leq \Delta\dot{\theta} \leq 60°\ . \tag{5.4}$$

We take 15 points in each axis and it results in 15^4 points in total. To specify the disrupt initial points that converge to a desired fixed-point, we use following condition

$$(\mathbf{X}_{end} - \mathbf{X}^*)^T W (\mathbf{X}_{end} - \mathbf{X}^*) < 0.01 \tag{5.5}$$

where W is a diagonal matrix whose entries are r_{td}^2, $g\, r_{td}$, 1 and 1. This weight matrix turns the state into a dimensionless quantity. If an initial point satisfies this constraint, it becomes an element of the basin of attraction.

Table 5.1: The states and control parameters of fixed-points on Table 5.2

	States				**Control Parameters**		
	z (m)	$\dot{x}$ (m/s)	θ (deg)	$\dot{\theta}$ (deg/s)	α_{td} (deg)	d_{vpp} (m)	θ_{vpp} (deg/s)
$\mathbf{X}^1$	1.18	5.42	0.00	6.61	115.61	0.1	0
$\mathbf{X}^2$	1.09	1.58	0.00	18.62	101.84	0.4	0
$\mathbf{X}^3$	1.25	2.63	1.04	5.01	105.40	0.1	-1
$\mathbf{X}^4$	1.57	2.48	-1.04	5.01	104.02	0.1	1

In Table 5.2, we show basin of attraction, settling time and $|\lambda|_{max}$ for the fixed-points on Table 5.1. We calculate the basin of attraction as (# of converged initial points)$/15^4$. The settling time is the first apex state that satisfies Eq. (5.5) while running. We only look the initial points that converges for all controllers. The settling time on Table 5.2 is the mean value obtained for a fixed point.

When we compare VPPC and PTC-L, we can see that while PTC-L offers consistently larger basins of attractions for all fixed points, there seems to be a relative drop in settling time performance. On the other hand, the PTC controller, which has one more extra control DOF than the other controllers, has the best performance among the three controllers in terms of both basin of attraction and settling time.

Note that one should expect to see a correlation between $|\lambda|_{max}$ and the settling performances, eigenvalues (or poles) dominantly determine the settling- and convergence-time values in linear dynamical systems. In that respect, settling time decreases as the $|\lambda|_{max}$ gets smaller, and vice versa. However, there are two discrepancies, which probably arise from nonlinearities. Although $|\lambda|_{max}$ of PTC is lower than $|\lambda|_{max}$ of VPPC, we can not see the same trend the settling time for $\mathbf{X}^2$. The reason might be that the nonlinearities dominate the dynamics. This also might explain why the basin of attraction values are significantly less than others. We observe another discrepancy in $\mathbf{X}^3$. We evaluate the settling time in Table 5.2 for the initial points that converge for all controllers. When we assess the settling time separately for each controller, we get 4.61 for VPPC, 3.47 for PTC, and 13.69 for PTC-L, which is consistent with the result in Table 5.2.

Table 5.2: Basin of attraction, settling time and $|\lambda|_{max}$ of the selected fixed-points

	Controllers / Fixed-points	VPPC	PTC	PTC-L
Basin of Attraction (%)	$\mathbf{X}^1$	3.38	22.72	27.14
	$\mathbf{X}^2$	1.09	3.68	2.14
	$\mathbf{X}^3$	6.52	17.61	22.00
	$\mathbf{X}^4$	7.67	16.09	18.57
Settling Time (# of apex)	$\mathbf{X}^1$	3.38	2.96	4.26
	$\mathbf{X}^2$	2.04	2.08	2.22
	$\mathbf{X}^3$	2.95	3.20	11.10
	$\mathbf{X}^4$	2.42	2.40	4.21
$\lvert\lambda\rvert_{max}$	$\mathbf{X}^1$	0.76	0.74	0.85
	$\mathbf{X}^2$	0.93	0.92	0.99
	$\mathbf{X}^3$	0.85	0.84	0.93
	$\mathbf{X}^4$	0.8	0.77	0.91

Fig. 5.4 and Fig. 5.5 are the cross-sections from the basin of attraction of $\mathbf{X}^3$. In Fig. 5.4, $\Delta\theta = \Delta\dot{\theta} = 0$. As seen, the controllers have roughly same basin of attraction. However, when we select $\Delta z = \Delta\dot{x} = 0$ and disturb the system in the direction of z and $\dot{x}$, the performance of VPPC significantly degrades which is not surprising according to Table 5.2.

Fig. 5.6 shows an example running simulation of $\mathbf{X}^1$ with the disturbance $\Delta z = 0$m, $\Delta\dot{x} = 0.3$m/s, $\Delta\theta = -2^\circ$. In this simulation VPPC cannot handle the disturbance, after three steps it fails. PTC and PTC-L shows similar performance except that PTC-L has higher convergence rate with respect to PTC. This result is compatible with the results from Table 5.2.

Fig. 5.7 and Fig. 5.8 show the ground reaction forces and the hip torque respectively. As expected, all three controllers perform differently from each other. Fig. 5.7 shows that PTC does not yield VPP. This flexibility gives better effectiveness while handling disturbances.

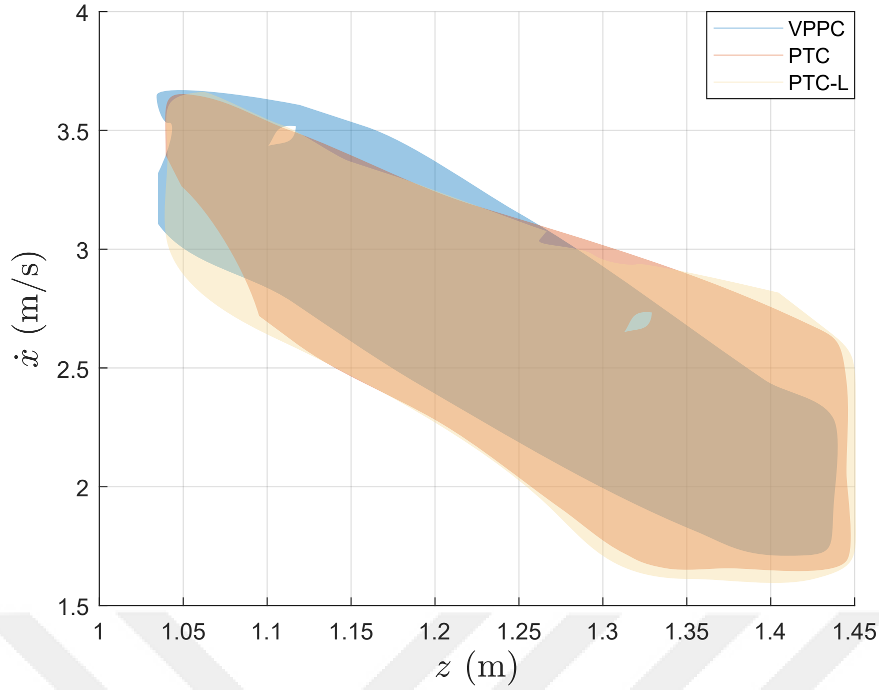

Figure 5.4: Basin of attraction of $\mathbf{X}^3$ when $\Delta\theta = \Delta\dot{\theta} = 0$.

To sum up, all controllers can successfully stabilize the system in the fixed-points neighborhood. PTC's performance is significantly better than that of other controllers based on both the basin of attraction and settling time criteria. PTC-L provides larger basins of attractions than VPPC, but it has a higher settling time values. Since the priority of locomotion is to avoid falling, one can choose PTC-L over VPPC. In short, PTC and PTC-L can be viable alternatives for controlling T-SLIP like systems. The only caveat is that PTC and PTC-L require the measurement/estimation of $\dot{r}$, which would bring a minor extra effort since all algorithms already depend on r and simple digital derivative blocks or trackers can easily estimate $\dot{\hat{r}}$.

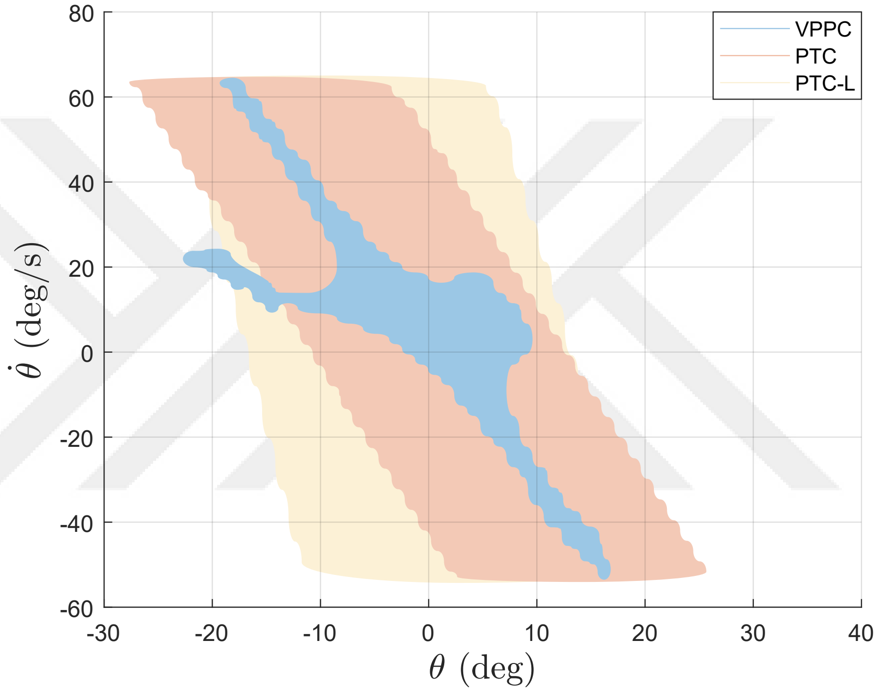

Figure 5.5: Basin of attraction of $\mathbf{X}^3$ when $\Delta z = \Delta \dot{x} = 0$.

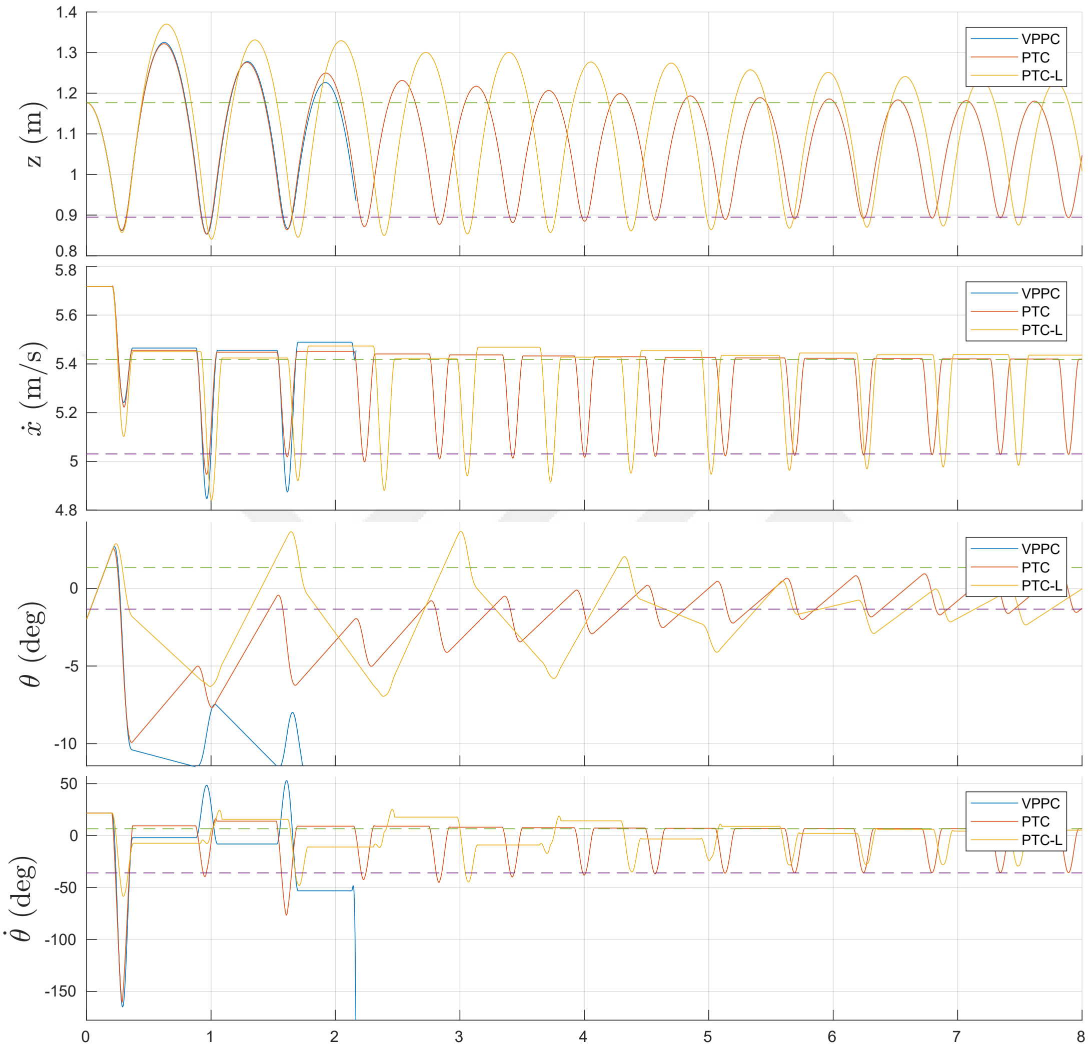

Figure 5.6: An example running simulation of $\mathbf{X}^1$ with the disturbance $\Delta z = 0$m, $\Delta \dot{x} = 0.3$m/s, $\Delta \theta = -2°$ and $\Delta \dot{\theta} = 15°$. The dashed lines represents minimum and maximum values of $\mathbf{X}^1$ while running without disturbance.

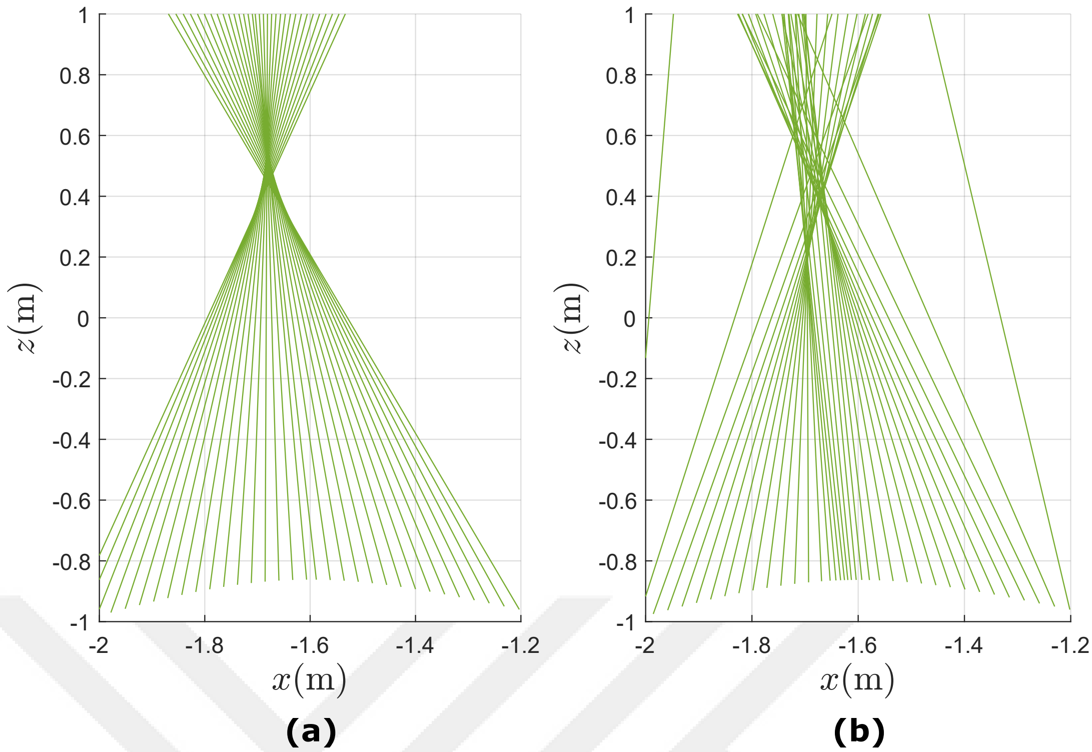

Figure 5.7: The ground reaction forces from the first stance phase in Fig. 5.6. **(a)** is VPPC, **(b)** is PTC.

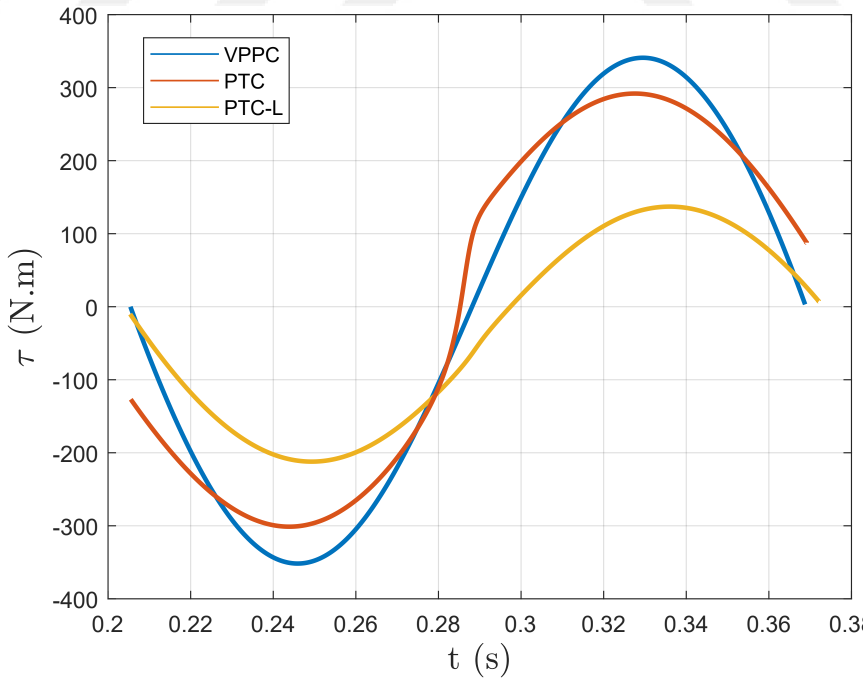

Figure 5.8: The torque profiles form the first stance phase in Fig. 5.6.

CHAPTER 6

CONCLUSIONS

The focal points of this thesis were the trunk extended SLIP model (T-SLIP), and the VPP scheme used to stabilize the model. We presented a systematic and detailed analysis if the VPP concept and T-SLIP model and later concentrated the feedback controller. In the first part of the thesis, we analyzed the existence and characteristics of the periodic solutions. Since it is theoretically impossible to find analytical solutions for T-SLIP trajectories [44], we adopted numeric tools for these analyses. We found out that the fixed-points of the system lie on a 1-dimensional manifold, and this manifold is parallel to height, z, axis. In this context, the system does not yield a limit cycle (passively) different from the SLIP model because periodic solutions are not isolated. We examined the existence and dependency of the fixed points with respect to the control parameters of the VPP. We derived the following conclusions:

- The control parameters have negligible effects on the apex height,
- The leg angle at touchdown, α_{td}, mostly affects the apex speed, $\dot{x}$,
- We can independently select the pitch angle, θ, by selecting proper θ_{VPP} without effecting the other states,
- d_{vpp} mostly affects the pitch rate, $\dot{\theta}$.

Thus, one can select different fixed-points by changing the system's control parameters based on the design requirements. On of the performance criterion that we focused on this paper is efficiency. We evaluated the cost of transport for all of the extracted periodic solutions so that we can analyze the fixed-points that provide better efficiency. The selection criteria can be summarized as follows:

- We have flexibility in selecting apex height, z. Since the cost of transport does not change with the apex and the other states lies in a small set for different apex heights on the 1-manifold,
- Low values of pitch rate, $\dot{\theta}$, and apex speed, $\dot{x}$, give a better cost of transport,
- When the body is perpendicular to the ground, $\theta = 0°$, the system has the best cost of transport.

In the second part of the thesis, we focused on the controllers since most fixed-points were unstable. We extended the controller previously developed by Sharbafi et al. [46] and developed a new controller called PTC. We showed that PTC outperforms VPPC based on the provided basin of attractions without compromising from the settling time performance. The only added cost of the new controller is that. it needs to measure $\dot{r}$ in addition to r for the control updates. However, it is a minor extra effort since both of the controllers already depend on r, and it relatively easy to estimate $\dot{r}$ from the measurements of r.

The existence of periodic solutions of the system and the ability to develop capable controllers for these periodic solutions pave the way for several future works. First of all, this concept with developed controllers can be used for real humanoid systems. In the near future, we plan to use the work presented in this thesis for a parsimonious humanoid system model in a simulation environment.

The next step after the simulation is to perform the work developed here on a real platform. A robot with similar physical characteristics to T-SLIP will make the implementation easier. In this context, ATRIAS is a good candidate. One can follow the steps in [34], where SLIP was used as a control target for ATRIAS, to implement the VPP concept in a platform similar to ATRIAS. In this work, they first calculate the necessary ground reaction forces to track SLIP trajectories and stabilize the trunk. And then, by using inverse dynamics, they evaluate the necessary torque output of the actuators. Instead of the first phase of the implementation, one can use the developed work here. Offline computation of the fixed-points of the VPP concept on the T-SLIP model with the corresponding A and B matrices can be loaded into the ATRIAS. And then, using this data, the ground reaction forces can be computed online. At every apex state, the controller parameters can be evaluated by using LQR, and the ground reaction force between two consecutive apex state can be evaluated by a numerical integration method. For the rest, the same process that is presented in [34] can be followed.

One of the open questions left in this thesis, and the literature is what should be the pitch angle in humanoid systems to achieve better efficiency and robustness. We found out that the body should be the upright position for the VPP concept on the T-SLIP model. However, it might not be the case if we use a lossy model that better accounts for real systems instead of the T-SLIP model.

In our work published recently [38], we show that if we choose a larger pitch angle in the positive direction than that dictated by the periodic solution, the energy of the system increases, and if we pick a negative pitch angle, the energy decreases on the T-SLIP model. Adding damping to the T-SLIP model can be a better control target for humanoid systems and yield promising results in terms of efficient pitch angle.

Another critical point that we would like to consider in the future is finding an approximate analytical relationship between the SLIP model and the VPP concept on the T-SLIP model. It could allow us to use the theoretical background developed for the SLIP model. Ultimately, our goal is to implement developed control schemes and possible future findings on a physical robot platform.

REFERENCES

[1] H.-M. Maus, S. Lipfert, M. Gross, J. Rummel, and A. Seyfarth, "Upright human gait did not provide a major mechanical challenge for our ancestors," *Nature communications*, vol. 1, p. 70, 2010.

[2] S. K. Thorpe, R. L. Holder, and R. H. Crompton, "Origin of human bipedalism as an adaptation for locomotion on flexible branches," *Science*, vol. 316, no. 5829, pp. 1328–1331, 2007.

[3] C. B. Stanford, "Arboreal bipedalism in wild chimpanzees: Implications for the evolution of hominid posture and locomotion," *American Journal of Physical Anthropology: The Official Publication of the American Association of Physical Anthropologists*, vol. 129, no. 2, pp. 225–231, 2006.

[4] H. Pontzer, D. A. Raichlen, and M. D. Sockol, "The metabolic cost of walking in humans, chimpanzees, and early hominins," *Journal of Human Evolution*, vol. 56, no. 1, pp. 43–54, 2009.

[5] M. D. Sockol, D. A. Raichlen, and H. Pontzer, "Chimpanzee locomotor energetics and the origin of human bipedalism," *Proceedings of the national academy of sciences*, vol. 104, no. 30, pp. 12265–12269, 2007.

[6] P. E. Wheeler, "The thermoregulatory advantages of hominid bipedalism in open equatorial environments: the contribution of increased convective heat loss and cutaneous evaporative cooling," *Journal of Human Evolution*, vol. 21, no. 2, pp. 107–115, 1991.

[7] A. Goswami and P. Vadakkepat, *Humanoid robotics: A reference*. Springer, 2019.

[8] M. Hirose and K. Ogawa, "Honda humanoid robots development," *Philosophical Transactions of the Royal Society A: Mathematical, Physical and Engineering Sciences*, vol. 365, no. 1850, pp. 11–19, 2007.

[9] M. Vukobratovic and D. Juricic, "Contribution to the synthesis of biped gait," *IEEE Transactions on Biomedical Engineering*, no. 1, pp. 1–6, 1969.

[10] J.-H. Kim, S.-W. Park, I.-W. Park, and J.-H. Oh, "Development of a humanoid biped walking robot platform khr-1-initial design and its performance evaluation," *feedback*, vol. 1, p. 12, 2002.

[11] S. Lohmeier, K. Loffler, M. Gienger, H. Ulbrich, and F. Pfeiffer, "Computer system and control of biped" johnnie"," in *IEEE International Conference on Robotics and Automation, 2004. Proceedings. ICRA'04. 2004*, vol. 4, pp. 4222–4227, IEEE, 2004.

[12] L. Geppert, "Qrio, the robot that could," *Ieee Spectrum*, vol. 41, no. 5, pp. 34–37, 2004.

[13] S. Collins, A. Ruina, R. Tedrake, and M. Wisse, "Efficient bipedal robots based on passive-dynamic walkers," *Science*, vol. 307, no. 5712, pp. 1082–1085, 2005.

[14] M. H. Raibert, *Legged robots that balance*. MIT press, 1986.

[15] R. Blickhan, "The spring-mass model for running and hopping," *Journal of biomechanics*, vol. 22, no. 11-12, pp. 1217–1227, 1989.

[16] W. SCHWIND, "Spring loaded inverted pendulum running: A plant model.," *PhD thesis, The University of Michigan, Dept. of EECS*, 1998.

[17] B. Brown and G. Zeglin, "The bow leg hopping robot," in *Proceedings. 1998 IEEE International Conference on Robotics and Automation (Cat. No. 98CH36146)*, vol. 1, pp. 781–786, IEEE, 1998.

[18] P. Gregorio, M. Ahmadi, and M. Buehler, "Design, control, and energetics of an electrically actuated legged robot," *IEEE Transactions on Systems, Man, and Cybernetics, Part B (Cybernetics)*, vol. 27, no. 4, pp. 626–634, 1997.

[19] M. H. Dickinson, C. T. Farley, R. J. Full, M. Koehl, R. Kram, and S. Lehman, "How animals move: an integrative view," *science*, vol. 288, no. 5463, pp. 100–106, 2000.

[20] T. Kubow and R. Full, "The role of the mechanical system in control: a hypothesis of self–stabilization in hexapedal runners," *Philosophical Transactions of*

the Royal Society of London. Series B: Biological Sciences, vol. 354, no. 1385, pp. 849–861, 1999.

[21] C. Li, T. Zhang, and D. I. Goldman, "A terradynamics of legged locomotion on granular media," *science*, vol. 339, no. 6126, pp. 1408–1412, 2013.

[22] R. J. Full and D. E. Koditschek, "Templates and anchors: neuromechanical hypotheses of legged locomotion on land," *Journal of experimental biology*, vol. 202, no. 23, pp. 3325–3332, 1999.

[23] M. Ahmadi and M. Buehler, "The arl monopod ii running robot: Control and energetics," in *Proceedings 1999 IEEE International Conference on Robotics and Automation (Cat. No. 99CH36288C)*, vol. 3, pp. 1689–1694, IEEE, 1999.

[24] A. Hereid, S. Kolathaya, M. S. Jones, J. Van Why, J. W. Hurst, and A. D. Ames, "Dynamic multi-domain bipedal walking with atrias through slip based human-inspired control," in *Proceedings of the 17th international conference on Hybrid systems: computation and control*, pp. 263–272, ACM, 2014.

[25] U. Saranli and D. E. Koditschek, "Template based control of hexapedal running," in *2003 IEEE International Conference on Robotics and Automation (Cat. No. 03CH37422)*, vol. 1, pp. 1374–1379, IEEE, 2003.

[26] M. M. Ankaralı and U. Saranlı, "Control of underactuated planar pronking through an embedded spring-mass hopper template," *Autonomous Robots*, vol. 30, no. 2, pp. 217–231, 2011.

[27] W.-C. Lu, M.-Y. Yu, and P.-C. Lin, "Clock-torqued rolling slip model and its application to variable-speed running in a hexapod robot," *IEEE Transactions on Robotics*, vol. 34, no. 6, pp. 1643–1650, 2018.

[28] T. Apgar, P. Clary, K. Green, A. Fern, and J. W. Hurst, "Fast online trajectory optimization for the bipedal robot cassie.," in *Robotics: Science and Systems*, vol. 101, 2018.

[29] A. Ramezani, J. W. Hurst, K. Akbari Hamed, and J. W. Grizzle, "Performance analysis and feedback control of atrias, a three-dimensional bipedal robot," *Journal of Dynamic Systems, Measurement, and Control*, vol. 136, no. 2, 2014.

[30] İ. Uyanık, Ö. Morgül, and U. Saranli, “Experimental validation of a feed-forward predictor for the spring-loaded inverted pendulum template,” *IEEE Transactions on robotics*, vol. 31, no. 1, pp. 208–216, 2015.

[31] N. T. Doan, T. Hayashi, and M. Yamakita, “High speed running of flat foot biped robot with inerter using slip model,” in *2015 IEEE International Conference on Advanced Intelligent Mechatronics (AIM)*, pp. 110–115, IEEE, 2015.

[32] N. Neville, M. Buehler, and I. Sharf, “A bipedal running robot with one actuator per leg,” in *Proceedings 2006 IEEE International Conference on Robotics and Automation, 2006. ICRA 2006.*, pp. 848–853, IEEE, 2006.

[33] N. Shemer and A. Degani, “Analytical control parameters of the swing leg retraction method using an instantaneous slip model,” in *2014 IEEE/RSJ International Conference on Intelligent Robots and Systems*, pp. 4065–4070, IEEE, 2014.

[34] W. C. Martin, A. Wu, and H. Geyer, “Experimental evaluation of deadbeat running on the atrias biped,” *IEEE Robotics and Automation Letters*, vol. 2, no. 2, pp. 1085–1092, 2017.

[35] I. Poulakakis and J. Grizzle, “Formal embedding of the spring loaded inverted pendulum in an asymmetric hopper,” in *2007 European Control Conference (ECC)*, pp. 3159–3166, IEEE, 2007.

[36] M. A. Sharbafi, C. Maufroy, M. N. Ahmadabadi, M. J. Yazdanpanah, and A. Seyfarth, “Robust hopping based on virtual pendulum posture control,” *Bioinspiration & biomimetics*, vol. 8, no. 3, p. 036002, 2013.

[37] G. Bayır, *Identification and stability analysis of periodic motions for a planar legged runner with a rigid body and a compliant leg*. PhD thesis, bilkent university, 2013.

[38] O. K. Karagoz, I. Sever, U. Saranli, and M. M. Ankarali, “Analysis and control of a body-attached spring-mass runner based on central pivot point approach,” in *2020 IEEE/ASME International Conference on Advanced Intelligent Mechatronics (AIM)*, pp. 495–500, IEEE, 2020.

[39] H.-M. Maus, J. Rummel, and A. Seyfarth, “Stable upright walking and running using a simple pendulum based control scheme,” in *International Conference of Climbing and Walking Robots*, pp. 623–629, 2008.

[40] K. G. Gruben and W. L. Boehm, “Force direction pattern stabilizes sagittal plane mechanics of human walking,” *Human movement science*, vol. 31, no. 3, pp. 649–659, 2012.

[41] J. W. Grizzle, G. Abba, and F. Plestan, “Asymptotically stable walking for biped robots: Analysis via systems with impulse effects,” *IEEE Transactions on automatic control*, vol. 46, no. 1, pp. 51–64, 2001.

[42] W. M. Haddad, V. Chellaboina, and S. G. Nersesov, *Impulsive and hybrid dynamical systems: stability, dissipativity, and control*, vol. 49. Princeton University Press, 2006.

[43] J. Seipel and P. Holmes, “A simple model for clock-actuated legged locomotion,” *Regular and chaotic dynamics*, vol. 12, no. 5, pp. 502–520, 2007.

[44] P. Holmes, “Poincaré, celestial mechanics, dynamical-systems theory and “chaos”,” *Physics Reports*, vol. 193, no. 3, pp. 137–163, 1990.

[45] M. M. Ankarali and U. Saranli, “Stride-to-stride energy regulation for robust self-stability of a torque-actuated dissipative spring-mass hopper,” *Chaos: An Interdisciplinary Journal of Nonlinear Science*, vol. 20, no. 3, p. 033121, 2010.

[46] M. A. Sharbafi, C. Maufroy, H. M. Maus, A. Seyfarth, M. N. Ahmadabadi, and M. J. Yazdanpanah, “Controllers for robust hopping with upright trunk based on the virtual pendulum concept,” in *2012 IEEE/RSJ International Conference on Intelligent Robots and Systems*, pp. 2222–2227, IEEE, 2012.

[47] M. A. Sharbafi, M. N. Ahmadabadi, M. J. Yazdanpanah, A. M. Nejad, and A. Seyfarth, “Compliant hip function simplifies control for hopping and running,” in *2013 IEEE/RSJ International Conference on Intelligent Robots and Systems*, pp. 5127–5133, IEEE, 2013.

[48] M. A. Sharbafi and A. Seyfarth, “Stable running by leg force-modulated hip stiffness,” in *5th IEEE RAS/EMBS International Conference on Biomedical Robotics and Biomechatronics*, pp. 204–210, IEEE, 2014.

[49] J. Rummel and A. Seyfarth, "Passive stabilization of the trunk in walking," *hip*, vol. 180, no. 190, p. 200, 2010.

[50] M. Ahmadi and M. Buehler, "Stable control of a simulated one-legged running robot with hip and leg compliance," *IEEE transactions on robotics and automation*, vol. 13, no. 1, pp. 96–104, 1997.

[51] A. Sato and M. Buehler, "A planar hopping robot with one actuator: design, simulation, and experimental results," in *2004 IEEE/RSJ International Conference on Intelligent Robots and Systems (IROS)(IEEE Cat. No. 04CH37566)*, vol. 4, pp. 3540–3545, IEEE, 2004.

[52] J. Rummel, Y. Blum, and A. Seyfarth, "Robust and efficient walking with spring-like legs," *Bioinspiration & biomimetics*, vol. 5, no. 4, p. 046004, 2010.

[53] O. K. Karagöz and M. M. Ankarali, "Optimization of physical parameters of an underactuated quadrupedal robot," in *2018 26th Signal Processing and Communications Applications Conference (SIU)*, pp. 1–4, IEEE, 2018.

[54] S. Seok, A. Wang, M. Y. Chuah, D. J. Hyun, J. Lee, D. M. Otten, J. H. Lang, and S. Kim, "Design principles for energy-efficient legged locomotion and implementation on the mit cheetah robot," *Ieee/asme transactions on mechatronics*, vol. 20, no. 3, pp. 1117–1129, 2014.

[55] W. Y. Yang, W. Cao, J. Kim, K. W. Park, H.-H. Park, J. Joung, J.-S. Ro, H. L. Lee, C.-H. Hong, and T. Im, *Applied numerical methods using MATLAB*. John Wiley & Sons, 2020.

[56] K. A. Hamed, B. G. Buss, and J. W. Grizzle, "Exponentially stabilizing continuous-time controllers for periodic orbits of hybrid systems: Application to bipedal locomotion with ground height variations," *The International Journal of Robotics Research*, vol. 35, no. 8, pp. 977–999, 2016.

[57] T. Cnops, Z. Gan, and C. D. Remy, "The basin of attraction for running robots: Fractals, multistep trajectories, and the choice of control," in *2015 IEEE/RSJ International Conference on Intelligent Robots and Systems (IROS)*, pp. 1586–1591, IEEE, 2015.

[58] R. M. Ghigliazza, R. Altendorfer, P. Holmes, and D. Koditschek, “A simply stabilized running model,” *SIAM review*, vol. 47, no. 3, pp. 519–549, 2005.

[59] K. A. Hamed and J. W. Grizzle, “Event-based stabilization of periodic orbits for underactuated 3-d bipedal robots with left-right symmetry,” *IEEE Transactions on Robotics*, vol. 30, no. 2, pp. 365–381, 2013.

[60] M. Buehler, D. E. Koditschek, and P. J. Kindlmann, “Planning and control of robotic juggling and catching tasks,” *The International Journal of Robotics Research*, vol. 13, no. 2, pp. 101–118, 1994.

[61] N. Lehtomaki, N. Sandell, and M. Athans, “Robustness results in linear-quadratic gaussian based multivariable control designs,” *IEEE Transactions on Automatic Control*, vol. 26, no. 1, pp. 75–93, 1981.

[62] G. C. Goodwin, S. F. Graebe, M. E. Salgado, *et al.*, *Control system design*. Upper Saddle River, NJ: Prentice Hall,, 2001.

[63] A. Wu and H. Geyer, “The 3-d spring–mass model reveals a time-based deadbeat control for highly robust running and steering in uncertain environments,” *IEEE Transactions on Robotics*, vol. 29, no. 5, pp. 1114–1124, 2013.

[64] A. Seyfarth, H. Geyer, M. Günther, and R. Blickhan, “A movement criterion for running,” *Journal of biomechanics*, vol. 35, no. 5, pp. 649–655, 2002.

[65] Ö. Arslan and U. Saranli, “Reactive planning and control of planar spring–mass running on rough terrain,” *IEEE Transactions on Robotics*, vol. 28, no. 3, pp. 567–579, 2012.

[66] J. W. Hurst, J. E. Chestnutt, and A. A. Rizzi, “Design and philosophy of the bimasc, a highly dynamic biped,” in *Proceedings 2007 IEEE International Conference on Robotics and Automation*, pp. 1863–1868, IEEE, 2007.

[67] J. W. Hurst, “The electric cable differential leg: a novel design approach for walking and running,” *International Journal of Humanoid Robotics*, vol. 8, no. 02, pp. 301–321, 2011.

[68] G. Secer and U. Saranli, “Control of planar spring–mass running through virtual

tuning of radial leg damping," *IEEE Transactions on Robotics*, no. 99, pp. 1–14, 2018.

[69] S. Heim and A. Spröwitz, "Beyond basins of attraction: Quantifying robustness of natural dynamics," *IEEE Transactions on Robotics*, vol. 35, no. 4, pp. 939–952, 2019.

[70] P. Zaytsev, W. Wolfslag, and A. Ruina, "The boundaries of walking stability: Viability and controllability of simple models," *IEEE Transactions on Robotics*, vol. 34, no. 2, pp. 336–352, 2018.

[71] G. Secer and U. Saranli, "Control of hopping through active virtual tuning of leg damping for serially actuated legged robots," in *2014 IEEE International Conference on Robotics and Automation (ICRA)*, pp. 4556–4561, IEEE, 2014.

[72] D. Logan, T. Kiemel, and J. J. Jeka, "Using a system identification approach to investigate subtask control during human locomotion," *Frontiers in computational neuroscience*, vol. 10, p. 146, 2017.

[73] S. Revzen and J. M. Guckenheimer, "Estimating the phase of synchronized oscillators," *Physical Review E*, vol. 78, no. 5, p. 051907, 2008.

Appendix A

DETAILS OF EQ. (2.2)

Before evaluating $D_q\psi$ and $D_q r$, we define intermediate variables which are

$$x_h = x - d_{hip}sin(\theta) \tag{A.1}$$

$$z_h = z - d_{hip}cos(\theta) \tag{A.2}$$

$$\alpha = atan2(x_h, z_h)\ . \tag{A.3}$$

x_h and z_h are the hip's position. Using these we can evaluate r and ψ as

$$r = \sqrt{x_h^2 + z_h^2} \tag{A.4}$$

$$\psi = \alpha + \theta + 90^\circ\ . \tag{A.5}$$

Then $D_q r = \frac{d\mathbf{q}}{dr}$ and $D_q\psi = \frac{d\mathbf{q}}{d\psi}$ are

$$D_q r = \begin{bmatrix} \frac{x-d_{hip}\sin(\theta)}{\sqrt{(x-d_{hip}\sin(\theta))^2+(z-d_{hip}\cos\theta)^2}} \\ \frac{z-d_{hip}\cos\theta}{\sqrt{(x-d_{hip}\sin\theta)^2+(z-d_{hip}\cos\theta)^2}} \\ \frac{d_{hip}(z\sin(\theta)-x\cos(\theta))}{\sqrt{(x-d_{hip}\sin\theta)^2+(z-d_{hip}\cos(\theta))^2}} \end{bmatrix} \tag{A.6}$$

$$D_q\psi = \begin{bmatrix} \frac{d_{hip}\cos(\theta)-z}{(x-d_{hip}\sin(\theta))^2+(z-d_{hip}\cos(\theta))^2} \\ \frac{x-d_{hip}\sin(\theta)}{(x-d_{hip}\sin(\theta))^2+(z-d_{hip}\cos(\theta))^2} \\ \frac{d_{hip}(-d_{hip}+x\sin(\theta)+z\cos(\theta))}{d_{hip}^2-2d_{hip}x\sin(\theta)-2d_{hip}z\cos(\theta)+x^2+z^2} + 1 \end{bmatrix}\ . \tag{A.7}$$

Appendix B

VPP FORMULA DERIVATION

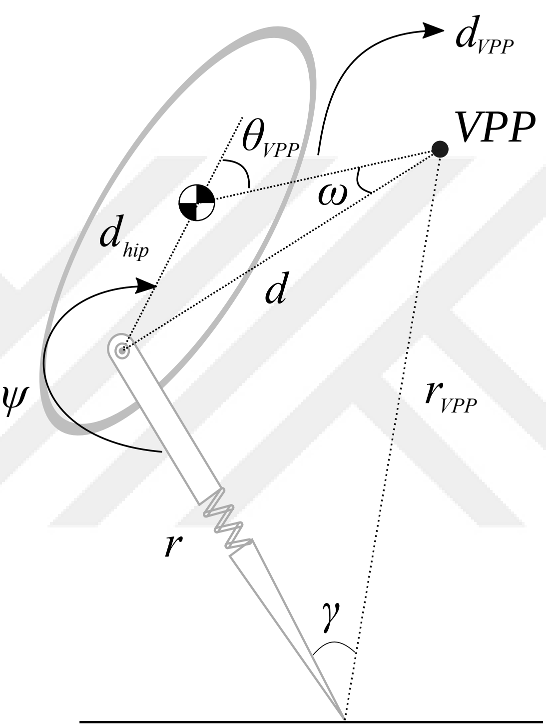

Figure B.1: T-SLIP model with VPP

The relation between τ_{VPP} and F_r is defined as

$$\tau_{VPP} = F_r r tan(\gamma)\ . \tag{B.1}$$

So we need to find $tan(\gamma)$. Let us define $\psi' = 360° - \psi$. From law of sines in the triangle defined by CoM, TD point and the hip:

$$sin(\gamma) = \frac{d}{r_{VPP}}\, sin(\psi' - \theta_{VPP} + \omega) \tag{B.2}$$

From law of cosines in the triangle defined by CoM, TD point and the hip:

$$cos(\gamma) = \frac{r^2 + r_{VPP}^2 - d^2}{2rr_{VPP}} \tag{B.3}$$

$$r_{VPP}^2 = d^2 + r^2 - 2drcos(\psi'\theta_{VPP} + \omega) \tag{B.4}$$

$$\tag{B.5}$$

Using Eq. (B.2), Eq. (B.3) and Eq. (B.4):

$$tan(\gamma) = \frac{2drsin(\psi' - \theta_{VPP} + \omega)}{2r^2 - 2drcos(\psi'\theta_{VPP} + \omega)} \tag{B.6}$$

From law of sines in the triangle defined by CoM, VPP and the hip:

$$sin(\theta_{VPP} - \omega) = \frac{d_{VPP}}{d} sin(\theta_{VPP}) \tag{B.7}$$

From law of cosines in the triangle defined by CoM, VPP and the hip:

$$cos(\theta_{VPP} - \omega) = \frac{d_{hip}^2 + d^2 - d_{hip}^2}{2d_{hip}d} sin(\theta_{VPP}) \tag{B.8}$$

$$d^2 = d_{hip}^2 + d_{VPP}^2 + 2d_{hip}d_{VPP}cos(\theta_{VPP}) \tag{B.9}$$

Using cosine difference of angles identity:

$$cos(\psi' - \theta_{VPP} + \omega) = cos(\psi')cos(\theta_{VPP} - \omega) + sin(\psi')sin(\theta_{VPP} - \omega) \tag{B.10}$$

Replacing suitable terms in Eq. (B.10) with Eq. (B.7), Eq. (B.8) and Eq. (B.9):

$$\begin{aligned} cos(\psi' - \theta_{VPP} + \omega) = cos(\psi')\frac{d_{hip} + d_{VPP}cos(\theta_{VPP})}{d} \\ + sin(\psi')sin(\theta_{VPP})\frac{d_{VPP}}{d} \end{aligned} \tag{B.11}$$

Using sine difference of angles identity:

$$sin(\psi' - \theta_{VPP} + \omega) = sin(\psi')cos(\theta_{VPP} - \omega) - cos(\psi')sin(\theta_{VPP} - \omega) \tag{B.12}$$

Replacing suitable terms in Eq. (B.12) with Eq. (B.7), Eq. (B.8) and Eq. (B.9):

$$\begin{aligned} sin(\psi' - \theta_{VPP} + \omega) = sin(\psi')\frac{d_{hip} + d_{VPP}cos(\theta_{VPP})}{d} \\ - cos(\psi')sin(\theta_{VPP})\frac{d_{VPP}}{d} \end{aligned} \tag{B.13}$$

Replacing suitable terms in Eq. (B.6) with Eq. (B.11) and Eq. (B.13):

$$tan(\gamma) = -\frac{d_{hip}sin(\psi') + d_{VPP}sin(\psi' - \theta_{VPP})}{z - d_{hip}cos(\psi') - d_{VPP}cos(\psi' - \theta_{VPP})} \tag{B.14}$$

Then,

$$\tau_{vpp} = F_r\ r\ \frac{d_{hip}\ sin(\psi) + d_{vpp}\ sin(\psi + \theta_{vpp})}{r - d_{hip}\ cos(\psi) - d_{vpp}\ cos(\psi + \theta_{vpp})}\ . \tag{B.15}$$